Universidade Estadual de Londrina

ALEXANDRE DE RAMOS ALABORA

COMPARATIVE STUDY BETWEEN DIFFERENT DARK MATTER HALO DENSITY PROFILES

Londrina, 12 de fevereiro de 2026

ALEXANDRE DE RAMOS ALABORA

COMPARATIVE STUDY BETWEEN DIFFERENT DARK MATTER HALO DENSITY PROFILES

Dissertação apresentada ao Departamento de Física da Universidade Estadual de Londrina, como requisito parcial à obtenção do título de Mestre em Física.

Orientadora: Prof^a. Mariana Penna Lima Vitenti

Londrina, 12 de fevereiro de 2026

Ficha de identificação da obra elaborada pelo autor, através do Programa de Geração Automática do Sistema de Bibliotecas da UEL

Alabora, Alexandre de Ramos.

COMPARATIVE STUDY BETWEEN DIFFERENT DARK MATTER HALO DENSITY PROFILES / Alexandre de Ramos Alabora. - Londrina, 26.
72 f. : il.

Orientador: Mariana Penna Lima Vitenti.
Dissertação (Mestrado em Física) - Universidade Estadual de Londrina, Centro de Ciências Exatas, Programa de Pós-Graduação em Física, 26.
Inclui bibliografia.

1. Matéria Escura - Tese. 2. Lenteamento Fraco - Tese. 3. Aglomerados de Galáxia - Tese. I. Vitenti, Mariana Penna Lima. II. Universidade Estadual de Londrina. Centro de Ciências Exatas. Programa de Pós-Graduação em Física. III. Título.

CDU 53

ALEXANDRE DE RAMOS ALABORA

COMPARATIVE STUDY BETWEEN DIFFERENT DARK MATTER HALO DENSITY PROFILES

Dissertação apresentada ao Departamento de Física da Universidade Estadual de Londrina, como requisito parcial à obtenção do título de Mestre em Física.

BANCA EXAMINADORA

Prof^a. Mariana Penna Lima Vitenti
Universidade de Brasília

Prof. Sandro Dias Pinto Vitenti
Universidade Estadual de Londrina

Prof^a. Cristina Furlanetto
Universidade Federal do Rio Grande do Sul

Londrina, 12 de março de 2026.

AGRADECIMENTOS

Muitas pessoas contribuíram, direta ou indiretamente, para a realização deste trabalho, e sou profundamente grato a todas elas.

Primeiramente, agradeço à Professora Dra. Mariana Penna Lima Vitenti, pela orientação, pela paciência, pelas discussões sempre valiosas e pelo apoio constante ao longo do desenvolvimento desta dissertação.

Agradeço também aos professores e alunos do grupo de cosmologia da UEL, que, entre aulas, reuniões e *Journal Clubs*, ajudaram a moldar minha visão da cosmologia e tornaram essa trajetória mais leve e enriquecedora. Agradeço, em particular, ao Prof. Dr. Sandro Dias Pinto Vitenti, que, além de ter contribuído para minha formação, realizou uma revisão atenciosa deste trabalho. Agradeço ainda à Profa. Dra. Cristina Furlanetto, da UFRGS, pelos apontamentos, conselhos e pela perspectiva valiosa compartilhada tanto na qualificação quanto na defesa.

Agradeço com carinho a Thais Mikami Ornellas e Ana Paula Bernabé Cavalaro, pela amizade, pela presença e pelo apoio ao longo dessa trajetória. Guardo com carinho as muitas viagens entre Maringá e Londrina, que se tornaram parte importante desse percurso.

À minha namorada, Mariana Esper Cheida Fernandes, deixo meu sincero agradecimento, pelo carinho, pela companhia, pela compreensão e pelo apoio em todos os momentos. Sua presença tornou esse caminho mais leve e mais feliz, mesmo nos períodos de maior cansaço e dificuldade.

Por fim, agradeço a todos que, de alguma forma, fizeram parte desta caminhada e contribuíram para que este trabalho pudesse ser realizado.

ALABORA, Alexandre. **Comparative Study Between Different Dark Matter Halo Density Profiles** 2026. **72**. Master's dissertation (Master in Physics) – State University of Londrina, Londrina, 2026.

ABSTRACT

Precise modeling of dark matter halo density profiles is increasingly important for mass calibration in modern cosmological surveys, where uncertainties in halo structure propagate into weak-lensing and cluster-based constraints on cosmology. This thesis reviews the ΛCDM framework, structure formation, and the role of halos in lensing analyses, and then compares several parametric halo density models within two widely used computational libraries: NumCosmo and Colossus. Using halos with a set of representative masses, $M_{\rm vir} \in \{5 \times 10^{13},\ 10^{14},\ 5 \times 10^{14},\ 10^{15}\}\ M_{\odot}$, at redshifts commonly explored in cosmological surveys, $z \in \{0.6,\ 0.9,\ 1.2\}$, we evaluate dark matter inner profiles (NFW, Hernquist, and Einasto), composite outer-profile extensions, and the DK14 model. The inner profiles show excellent agreement, with relative differences at the 10^{-9} to 10^{-8} level. The Einasto profile combined with constant-density and power-law outer terms also shows similarly high consistency, with discrepancies remaining at the 10^{-9} level once the normalization procedures are matched. The DK14 comparison yields agreement at the 10^{-7} level, indicating robust consistency even for a more structurally complex profile. In contrast, the Einasto + 2-halo comparison remains well behaved only over part of the radial range and develops significant discrepancies at large radii, showing that this case still requires further investigation. Overall, the results validate the NumCosmo implementations for the inner, mean-density, power-law, and DK14 profiles, while identifying the 2-halo treatment as the main remaining source of unresolved numerical mismatch.

Keywords: Dark Matter, Halo, Weak Lensing, Galaxy Clusters, Cosmological Parameters.

ALABORA, Alexandre. **Estudo Comparativo Entre Diferentes Perfis de Densidade de Halos de Matéria Escura** 2026. **72**. Dissertação de mestrado (Mestrado em Física) – Universidade Estadual de Londrina, Londrina, 2026.

RESUMO

A modelagem precisa dos perfis de densidade de halos de matéria escura é cada vez mais importante para a calibração de massa em levantamentos cosmológicos modernos, nos quais incertezas na estrutura dos halos se propagam para restrições cosmológicas baseadas em lenteamento fraco e em aglomerados de galáxias. Esta dissertação revisa o arcabouço ΛCDM, a formação de estruturas e o papel dos halos em análises de lenteamento, e então compara diversos modelos paramétricos de densidade de halos em duas bibliotecas computacionais amplamente utilizadas: NumCosmo e Colossus. Utilizando halos com um conjunto de massas representativas, $M_{\rm vir} \in \{5\times10^{13},\ 10^{14},\ 5\times10^{14},\ 10^{15}\}\ M_\odot$, em redshifts comumente explorados em levantamentos cosmológicos, $z \in \{0.6,\ 0.9,\ 1.2\}$, avaliamos perfis internos de matéria escura (NFW, Hernquist e Einasto), extensões compostas para os perfis externos e o modelo DK14. Os perfis internos apresentam excelente concordância, com diferenças relativas no nível de 10^{-9} a 10^{-8}. O perfil de Einasto combinado com termos externos de densidade média constante e lei de potência também mostra consistência igualmente elevada, com discrepâncias permanecendo no nível de 10^{-9} uma vez compatibilizados os procedimentos de normalização. A comparação com o perfil DK14 apresenta concordância no nível de 10^{-7}, indicando robustez mesmo para um modelo estruturalmente mais complexo. Em contraste, a comparação do perfil de Einasto com o termo de 2-halos permanece bem comportada apenas em parte do intervalo radial e desenvolve discrepâncias significativas em grandes raios, mostrando que esse caso ainda requer investigação adicional. De modo geral, os resultados validam as implementações do NumCosmo para os perfis internos, para os termos externos de densidade média e lei de potência, e para o perfil DK14, ao mesmo tempo em que identificam o tratamento do termo de 2-halos como a principal fonte remanescente de incompatibilidade numérica.

Palavras-chave: Matéria Escura, Halo, Lenteamento Fraco, Aglomerados de Galáxias, Parâmetros Cosmológicos.

Contents

INTRODUCTION

The standard cosmological model, ΛCDM, successfully describes the large scale evolution of the Universe and the growth of structure from primordial density perturbations. On sufficiently large scales and at early times, when density fluctuations remain in the linear or weakly nonlinear regime, the predictions of ΛCDM are robust and well understood. However, on smaller scales nonlinear gravitational effects become dominant, and cold dark matter collapses hierarchically into gravitationally bound structures. Although these scales contain relevant statistical information, there is no general analytical solution available for nonlinear gravitational collapse.

To explore the nonlinear regime, we resort to a simplifying abstraction: the halo model. In this framework, all matter is distributed into individual dark matter halos that host galaxies and clusters of galaxies, so that all structure can be seen as the superposition of halos, providing the basic building blocks of the cosmic web. Three main ingredients define the halo model: the halo mass function (how many halos of a given mass we expect to find in a given region), bias (how the spatial distribution of halos correlates with the underlying linear density field), and a density profile (how matter or discrete tracers are distributed inside each halo). The non linear problem is then reduced to understanding how halos correlate with the matter field and with each other.

The advantages of the Halo Model come from the fact that its key ingredients can be calibrated against cosmological N-body simulations, which provide a controlled numerical realization of nonlinear gravitational collapse. Quantities can be measured across a range of masses, redshifts, and cosmological parameters, allowing the halo model to connect simulations to analytical predictions. At the same time, the accuracy of halo model predictions is directly tied to how well these ingredients capture the true structure of simulated and observed halos.

Cosmological observables such as galaxy clustering, weak gravitational lensing, and cluster abundance are all sensitive to how matter is distributed within these halos on small scales. In practice, cosmological surveys often do a scale cutoff in their analysis where the modeling is less reliable, effectively discarding information. As current and upcoming large surveys, e.g. Kilo-Degree Survey (KiDS) [1], Dark Energy Survey (DES) [2], Hyper Suprime Cam (HSC) [3], Legacy Survey of Space and Time (LSST) [4], deliver increasingly precise measurements, uncertainties in the internal structure of dark matter halos become a factor in the inference of galaxy cluster masses, and consequentially in cosmological parameters.

Particularly, the halo density profile dominates small scales when it comes to gravitational lensing effects. In galaxy–galaxy lensing, the tangential shear signal around lenses is directly sensitive to the projected mass distribution of their host halos, making halo profiles a key ingredient in cluster mass calibration. A recent development models not only the inner halo structure but also by the transition to the surrounding large scale matter distribution. As the statistical precision and angular resolution of weak lensing measurements improve with each generation of surveys, these outer profile effects become increasingly relevant.

In practice, halo density profiles and their lensing predictions are implemented in publicly available cosmological libraries that are widely used in the community. These tools enable fast and reproducible predictions and have become increasingly integrated into analysis pipelines. However, any numerical implementation necessarily involves choices in parametrization, normalization conventions, numerical integration strategies, etc. Such choices can lead to subtle but non negligible differences in predicted lensing signals and inferred halo masses, hence the importance of independent implementations to avoid introducing any new systematics in the analysis. Uniform definitions, transparent conventions, and cross-validation between publicly available libraries are essential to ensure reproducibility and to guarantee that theoretical predictions remain robust across independent implementations.

This thesis aims to review halo density profiles proposed in the literature and to compare their implementation in different computational tools. The main goal is to assess the level of agreement between independent implementations.

This work is organized as follows:

- **Chapter 1** presents the standard cosmological framework, the ΛCDM, detailing the background expansion, linear perturbations, and the key parameters that characterize the contents and evolution of the Universe.

- **Chapter 2** focuses on the formation of structure and the emergence of dark matter halos, introducing the spherical collapse model, halo mass functions, bias, and the halo model as a statistical description of the nonlinear matter distribution.

- **Chapter 3** develops the theoretical foundations of gravitational lensing, from the thin lens approximation to cosmic shear, and connects lensing observables to the underlying matter field and to cosmological surveys.

- **Chapter 4** introduces the dark matter halo density profiles that are the central objects of this study, comparing different parametric models, their physical interpretation, and their role in mass estimation.

- **Chapter 5** presents the implementation and validation of these profiles within two cosmological libraries, along with initial numerical results and comparison benchmarks.

- **Chapter 6** presents the conclusions of this work and discusses further developments, including possible improvements to the modeling, extensions of the analysis, and prospective cosmological applications.

1 THE STANDARD MODEL OF COSMOLOGY

Cosmology is the scientific study of the origin, composition, and evolution of the Universe as a whole. It is built upon the framework of General Relativity (GR), where the dynamics of the geometry of spacetime metric $g_{\mu\nu}$ are dictated by its matter-energy content, as described by the Einstein Field Equations (EFEs) [5]

$$R_{\mu\nu} - \frac{1}{2}Rg_{\mu\nu} + \Lambda g_{\mu\nu} = \frac{8\pi G}{c^4}T_{\mu\nu}, \tag{1.1}$$

the term $R_{\mu\nu} - \frac{1}{2}Rg_{\mu\nu}$ combine the Ricci Tensor and the Ricci Scalar to encode the differential geometry of the theory, $T_{\mu\nu}$ is the stress-energy tensor that describes the density and flow of energy and momentum, and finally $\Lambda g_{\mu\nu}$ accounts for the accelerated expansion rate driven by the cosmological constant Λ.

1.1 Homogeneous and Isotropic Background

Within this theoretical foundation the dynamics of the entire Universe can be described by assuming the Cosmological Principle, which states that on the very large scales the Universe is homogeneous and isotropic, that is, it appears the same in all directions and at all locations.

The spacetime geometry that satisfies these symmetries is given by the Friedmannn-Lemaître-Robertson-Walker (FLRW) metric [5]

$$ds^2 = -c^2dt^2 + a^2(t)\left[\frac{dr^2}{1-kr^2} + r^2(d\theta^2 + \sin^2\theta\, d\phi^2)\right], \tag{1.2}$$

in comoving spherical coordinates, $a(t)$ is the scale factor as a function of cosmic time t, and k is the spatial curvature constant ($k = 0, +1, -1$ for flat, closed and open universes respectively). This provides a general description of an expanding or contracting homogeneous and isotropic Universe. We can also approximate the matter-energy content of the Universe by a perfect fluid in the scales where the cosmological principle holds. In this case [5]

$$T_{\mu\nu} = \left(\rho + \frac{p}{c^2}\right)u_\mu u_\nu + pg_{\mu\nu}, \tag{1.3}$$

where u^μ the four-velocity of the fluid, satisfying $u^\mu u_\mu = -c^2$, p the pressure, and ρ is the energy density. This tensor represents a homogeneous and isotropic fluid, at rest in the cosmic frame of reference, exerting the same pressure in all directions and having no shear or viscosity.

When the Einstein Field Equations (Eq. 1.1) are solved under the conditions imposed by the FLRW metric with a perfect fluid as the source, they yield the Friedmann Equations [5]

$$\left(\frac{\dot{a}}{a}\right)^2 = \frac{8\pi G}{3}\rho - \frac{kc^2}{a^2} + \frac{\Lambda c^2}{3}, \tag{1.4}$$

$$\frac{\ddot{a}}{a} = -\frac{4\pi G}{3}\left(\rho + \frac{3p}{c^2}\right) + \frac{\Lambda c^2}{3}, \tag{1.5}$$

the first Eq. 1.4 arises from the time-time component and governs the rate of expansion through the Hubble parameter

$$H \equiv \frac{\dot{a}}{a}, \tag{1.6}$$

while Eq. (1.5), follows from the spatial components, and determines whether the expansion accelerates or decelerates. These equations relate the expansion rate of the Universe to its energy content, and form the basis of modern cosmology describing how different matter-energy components govern the evolution of the scale factor through time.

What dictates this evolution is how density ρ and pressure p behave. Using the first Friedmann Equation (1.4) we can rewrite the second Eq. 1.5 as [6]

$$\dot{\rho} = -3\frac{\dot{a}}{a}\left(\rho + \frac{p}{c^2}\right). \tag{1.7}$$

To close the system, a relation between pressure and density must be specified, an equation of state, typically assuming the form of a barotropic fluid, written as [6]

$$p = w\rho c^2, \tag{1.8}$$

where w is the dimensionless parameter that characterizes each component of the cosmic fluid. The solution of differential Eq. 1.7 with this equation of state, produces a proportionality relation between ρ and a in the form

$$\rho(a) = \rho_0\left(\frac{a_0}{a}\right)^{3(1+w)} \Rightarrow \rho(a) \propto a^{-3(1+w)}. \tag{1.9}$$

Specifying w for each component allows one to integrate Eq. 1.7 and determine how the energy density ρ evolves with the scale factor $a(t)$, thereby dictating the overall dynamics of cosmic expansion. Possibilities for w are summarized in [6] Table 1.1.

Table 1.1: Typical equation-of-state parameters for different cosmic components.

Component	$\rho(a) \propto$	w	**Intuition**
Non-relativistic matter (dust)	a^{-3}	0	Energy density diluted only by the increase in volume.
Radiation / relativistic particles	a^{-4}	1/3	Extra a^{-1} factor from wave energy loss in addition to volume dilution.
Cosmological constant (dark energy)	const.	-1	Constant vacuum energy that drives accelerated expansion.
Curvature term (effective)	a^{-2}	-1/3	Acts as a geometric contribution to total energy density.

We can rewrite the first Friedmann equation in a more practical form by defining the critical density as the density that results in a spatially flat universe $k = 0$ when $\Lambda = 0$

$$\rho_c \equiv \frac{3H^2}{8\pi G}, \tag{1.10}$$

we can then define the density parameter for each component (matter, radiation, dark energy) i as the ratio of its energy density to the critical density

$$\Omega_i := \frac{\rho_i}{\rho_c}. \tag{1.11}$$

We are interested in the present day values of these expressions, here denoted by a subscript 0

$$\rho_{c,0} = \frac{3H_0^2}{8\pi G}, \qquad \Omega_{i0} = \frac{\rho_{i0}}{\rho_{c,0}}. \tag{1.12}$$

Each component's density evolves with the scale factor a according to its equation of state

$$\rho_m(a) = \rho_{m0}a^{-3}, \qquad \rho_r(a) = \rho_{r0}a^{-4}, \qquad \rho_\Lambda(a) = \rho_{\Lambda 0} = \text{constant}. \tag{1.13}$$

Substituting these into the first Friedmann equation gives the dimensionless form [6]

$$\frac{H^2(a)}{H_0^2} = \Omega_{r0}\, a^{-4} + \Omega_{m0}\, a^{-3} + \Omega_{k0}\, a^{-2} + \Omega_{\Lambda 0}, \tag{1.14}$$

where $\Omega_{k0} \equiv -kc^2/H_0^2$ is the curvature density parameter today.

Writing the Equation this way, allow us to directly compare the relative contributions of each component to the overall dynamics and geometry of the Universe. Different choices of the density parameters lead to different cosmic histories (Fig. 1.1), corresponding to universes that expand forever or re-collapse, with the static scenario being unstable.

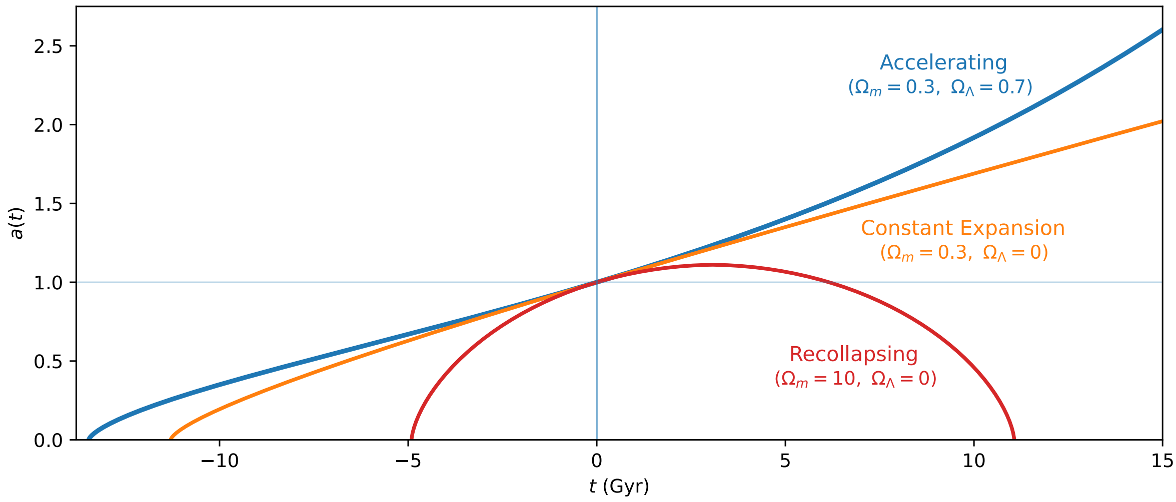

Figure 1.1: Evolution of the cosmic scale factor $a(t)$ illustrating some possible cosmic fates under different density parameter combinations. The present epoch corresponds to $t = 0$ with normalized to be $a(t = 0) = 1$.

Determining which of these scenarios describes our Universe requires observational constraints on the present-day values of the parameters.

1.2 Perturbations to the Background Cosmology

On sufficiently large scales we can approximate the Universe as homogeneous and isotropic. However, this approximation does not hold locally: matter and radiation distribute unevenly, giving rise to a rich hierarchy of structures, such as galaxies, stars, planets, and even living observers. We can model these inhomogeneities in the matter field by introducing small deviations to the background density in the early Universe that evolve under the influence of gravity.

While a full derivation is outside of the scope of this work, we outline here the general guideline to model such perturbations, closely following the treatment given by [6]. We consider the dynamics of a perfect fluid subject to gravity in an expanding background, adding small perturbations to describe their evolution. The dynamics of the system is given by the continuity and Euler equation from fluid dynamics, and the Poisson equation for the gravitational potential from the Newtonian theory, forming a coupled set of differential equations. Table 1.2 for comparison shows the equations and variables in their usual form and after the transformations necessary adding gravity in an expanding background.

Table 1.2: Comparison between the standard fluid equations and their cosmological (expanding universe) counterparts.

	Static Fluid		Cosmological Form	Effect
Coordinates	$\boldsymbol{r}(t)$	$\longrightarrow$	$\boldsymbol{r}(t) = a(t)\boldsymbol{x}$	Position in comoving coordinates.
Velocity	$\boldsymbol{u}(t)$	$\longrightarrow$	$\boldsymbol{u}(t) = \dot{\boldsymbol{r}} = H\boldsymbol{r} + \boldsymbol{v}$	Includes Hubble flow and peculiar motion.
Continuity	$\frac{\partial \rho}{\partial t} + \nabla \cdot (\rho \boldsymbol{u}) = 0$	$\longrightarrow$	$\frac{\partial \rho}{\partial t} + 3H\rho + \frac{1}{a}\nabla \cdot (\rho \boldsymbol{u}) = 0$	Density diluted by expansion.
Euler	$\rho\left(\frac{\partial}{\partial t} + \boldsymbol{u} \cdot \nabla\right)\boldsymbol{u} = -\nabla P$	$\longrightarrow$	$\left(\frac{\partial}{\partial t} + \boldsymbol{v} \cdot \nabla\right)\boldsymbol{u} = -\frac{1}{a}\frac{\nabla P}{\rho} - \frac{1}{a}\nabla\Phi$	Expansion adds damping, gradients scale as $1/a$.
Poisson	$\nabla^2\Phi = 4\pi G\rho$	$\longrightarrow$	$\nabla^2\Phi = 4\pi G a^2 \rho$	Potential scaled by a^2.

In fact, the solution for the coupled differential equations shown in Table 1.2 can only be consistent if the scale factor $a(t)$ satisfy the second Friedmann equation (Eq. 1.5), which is the background dynamics we discussed in the last section 1.1. We can now introduce small perturbations δ to the quantities on Table 1.2, and find their dynamics as well

$$\rho = \bar{\rho} + \delta\bar{\rho}, \qquad p = \bar{p} + \delta\bar{p}, \qquad \Phi = \bar{\Phi} + \delta\bar{\Phi}, \tag{1.15}$$

where the barred quantities represent the average background values. We define then the matter density contrast, that indicates for each region of space, how much its density deviates from the average

$$\delta = \frac{\rho - \bar{\rho}}{\bar{\rho}} = \frac{\delta\rho}{\bar{\rho}}. \tag{1.16}$$

We can define the dynamics of this contrast solving the equations of the Table 1.2 for the perturbed quantities, and an important assumption here is that $\delta \ll 1$, so that the second order terms can be ignored and the equations linearized. This yields [6]

$$\ddot{\delta} + 2H\dot{\delta} - \left(\frac{c_s^2}{a^2}\nabla^2 + 4\pi G\bar{\rho}\right)\delta = 0, \tag{1.17}$$

where the term $c_s^2/a^2\nabla^2\delta$ is the sound speed term accounting for pressure gradients.

The statistical properties of the density contrast field are of great interest for cosmology, since by definition the mean value is $\langle\delta\rangle = 0$. The next measurement is the two-point statistics

$$\xi(|\mathbf{x} - \mathbf{x}'|,\, t) \equiv \langle\delta(\mathbf{x}, t)\delta(\mathbf{x}', t)\rangle, \tag{1.18}$$

under homogeneity and isotropy ξ is invariant to translations and rotations, so it only depends on the separation between 2 points $\boldsymbol{r} = |\mathbf{x} - \mathbf{x}|'$. Additionally, the expected value $\langle\ \rangle$ represents the ensemble average over all possible realizations of the field $\delta(\boldsymbol{x}, t)$. In functional form this is written as [6]

$$\xi(|\boldsymbol{x} - \boldsymbol{x}'|, t) \equiv \langle\delta(\boldsymbol{x}, t)\,\delta(\boldsymbol{x}', t)\rangle = \int \mathcal{D}\delta\;\mathbb{P}[\delta]\,\delta(\boldsymbol{x}, t)\,\delta(\boldsymbol{x}', t). \tag{1.19}$$

Where $\mathcal{D}\delta$ is shorthand for integrating over all possible configurations of the field, and $\mathbb{P}[\delta]$ is the probability functional that encodes the stochastic behavior that creates the field. We will discuss later that for our Universe this probability matches a gaussian random field.

Is useful to define the two-point correlation function in the Fourier space

$$\langle \delta(\boldsymbol{k})\, \delta^*(\boldsymbol{k}') \rangle = (2\pi)^3 \delta_D(\boldsymbol{k} - \boldsymbol{k}') \int \mathrm{d}^3 r e^{-i\boldsymbol{k}\cdot\boldsymbol{r}} \xi(r) = (2\pi)^3 \delta_D(\boldsymbol{k} - \boldsymbol{k}')\, \mathcal{P}(k), \tag{1.20}$$

here δ_D is de Dirac delta function defined as

$$\delta_D(\boldsymbol{k} - \boldsymbol{k}') = \int \frac{\mathrm{d}\boldsymbol{x}^3}{(2\pi)^3} \exp\left[i\mathbf{x} \cdot (\boldsymbol{k} - \boldsymbol{k}')\right]. \tag{1.21}$$

$\mathcal{P}$ is called the power spectrum. The physical meaning of $\xi(\boldsymbol{r})$ is a measure of how likely it is to find two overdensities separated by a distance r compared to a random uncorrelated distribution

- $\xi(r) > 0$: correlation, overdensities tend to cluster at that separation;
- $\xi(r) = 0$: points are uncorrelated (random);
- $\xi(r) < 0$: anti-correlation, void like separation.

The power spectrum $\mathcal{P}(k)$ describes the amplitude of fluctuations as a function of scale,

- Large k (small scales): short wavelength, correspond to the finer structures of the field;
- Small k (large scales): long wavelength, describe broader slowly varying structures.

The correlation function ξ is straightfoward to measure observationally, while $\mathcal{P}$ is easier to predict theoretically [6], both of them are equivalent via the definition in Eq. 1.20.

It is natural to compute the ensemble averages to probe theories by varying their initial conditions, but so far we think only one realization of our Universe happened, giving us only one data point. Fortunately, we can assume ergodicity, which states that ensemble averages are equivalent to spatial averages as the volume becomes infinetely large. For a gaussian random field this is true as $\xi(r) \to 0$ for $r \to \infty$ [6]. So we can probe different far apart regions of the Universe as different realizations of the same underlying random process if we take into account sample variance.

Key assumptions were made in this development: Newtonian Gravity and Linear Perturbation. This is not the general case, in some contexts a full relativistic perturbative treatment should be used with the EFEs (Eq. 1.1) instead of the Poisson equation for gravity, and in others the evolution behave non linearly. We will discuss the specifics of which regimes these approximations are valid, and point out the occasions in which they are not in the coming Section.

1.3 The ΛCDM model of Cosmology

The most successful and widely accepted framework is the Λ Cold Dark Matter (ΛCDM) model. In this model, the Universe is flat ($k = 0$), and the expansion of the Universe is governed primarily by a cosmological constant Λ, associated with dark energy, and by Cold Dark Matter (CDM), a non-relativistic form of matter that interacts only through gravity. Together with baryonic matter and radiation, these components fully specify the evolution of the cosmic scale factor through Eq. 1.14.

Recent observations yield the following best-fit parameters for the variables in the Friedmann equation 1.14:

$$\begin{aligned}
&H_0 = 67.74 \pm 0.46 \,\mathrm{km\,s^{-1}\,Mpc^{-1}},\\
&\Omega_{CDM} = 0.264 \pm 0.004,\\
&\Omega_b = 0.0493 \pm 0.0006,\\
&\Omega_\Lambda = 0.6847 \pm 0.0073,\\
&\Omega_r = (9.02 \pm 0.21) \times 10^{-5},\\
&|\Omega_k| < 0.005,
\end{aligned} \tag{1.22}$$

these values are the results from 2018 from the Planck Collaboration [7]. According to these numbers our Universe is expanding at an accelerated rate closely following the blue line in Fig. 1.1.

Also, the mix of CDM, baryonic matter, radiation and dark energy gives us an unique picture of the general theory of perturbations described in the last section, where we can predict the transformations these components went through with the evolution of the scale factor $a(t)$, and observational imprints left by these events. The scaling behaviors of each component defined in Eq. 1.13 dictate a sequence of cosmic epochs. In the next paragraphs we conceptually outline the basic mechanisms in play in each epoch, and at the end of the discussion Fig. 1.3 pin points these events to the cosmic timeline.

The early Universe was dominated by radiation due to its high density and temperature. The energy density of relativistic particles scaled as $\rho_r \propto a^{-4}$ decreasing faster than matter. During this epoch radiation pressure prevented the gravitational collapse of overdense regions in the linear scenario described in section 1.2 [6], the resulting equation (Eq. 1.17) has a pressure term contraposing the gravitational one, but because we are dealing with relativistic species, a full relativistic treatment is due to get the correct picture.

Another crucial physical effect to take into account is: at this time matter and radiation were tightly coupled, forming a single relativistic fluid. Due to the short mean path photons had available, they scattered of of free eletrons via Thomson scattering, coupling radiation to baryonic inertia. At this period the Universe was opaque, but as it expanded and cooled, protons and eletrons combined to form neutral hydrogem atoms in a process called recombination [6]. This decoupled photons from baryonic matter allowing light to move freely, we observe the relic radiation from this epoch today as the Cosmic Microwave Background (CMB) (Fig 1.2), as nearly perfect blackbody spectrum at $T = 2.725$ K [7], carrying the imprint of the density fluctuations at the last scattering moment.

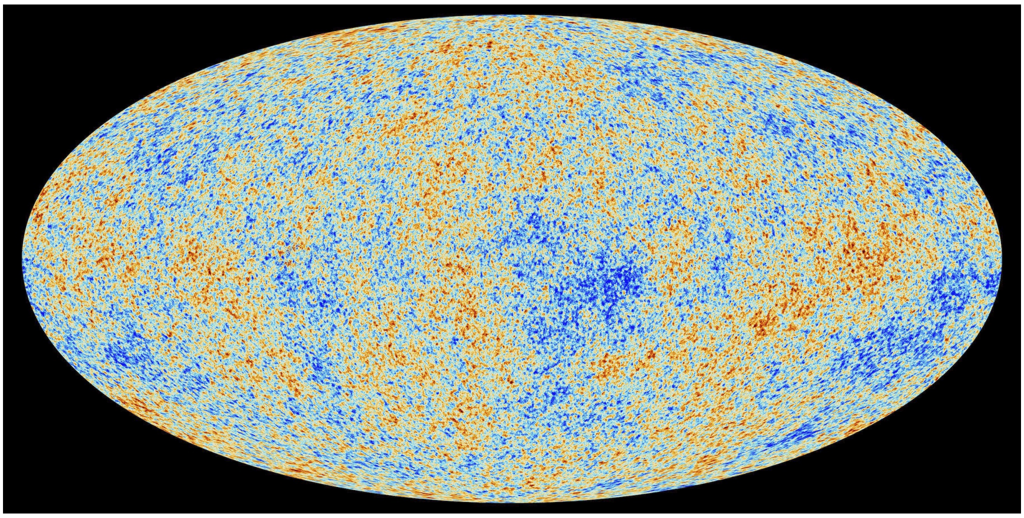

Figure 1.2: Temperature map of the cosmic microwave background measured by the Planck spacecraft. Source: [8]

Cold Dark Matter on the other hand, is collisionless and non-relativistic in nature, and it scales as $\rho_{CDM} \propto a^{-3}$, leading to the gradual dominance of matter after the radiation era. This scenario is well describe by the linear perturbation regime at large scales [6]. Being weakly interacting, CDM started to clump gravitationally well before baryons decoupled from photons, seeding the potential wells that would later attract ordinary matter. These early inhomogeneities, preserved through cosmic expansion, form the backbone of the large scale structure observed today.

After decoupling, baryonic matter followed the exiting peaks an troughs of the density field already set in place by CDM. The decoupled baryons amplified the existing density contrast accelerating the process of structure formation [6]. Over time these overdense regions collapsed to form stars and galaxies, being the astrophysical tracers of matter we see in the night sky.

Finally, at late times, the cosmological constant Λ associated with dark energy, began to dominate the total energy density. Unlike matter and radiation, its density remains constant as the Universe expands ($\rho_\Lambda = \text{const.}$), driving the observed accelerated expansions and the slowing in structure growth [6]. This transition marks the onset of the dark energy dominated epoch, during which the scale factor evolves exponentially with time.

To better construct a visual timeline of these events we introduce the concept of cosmological redshift z. Photons moving in an expanding background undergo the Doppler Effect increasing its wavelength (moving it to the red direction of the spectrum). This cosmological redshift can be written as a function of a

$$1 + z = \frac{a_0}{a(t)}. \tag{1.23}$$

This is very useful, observationally we can measure, for example, the redshift of close and distant galaxies, and of the CMB itself [6]. Redshift is commonly used to label events in the history of the Universe. We can also recover the cosmic time a photon was emitted from its source using the lookback time, defined as

$$t_L(z) = \frac{1}{H_0}\int_0^z dz' \, \frac{1}{(1+z')E(z')} \tag{1.24}$$

Here $E(z)$ is the dimensionless Friedman equation 1.14 written in terms of z, expliciting the dependence in the chosen cosmological model, and $t_L(z)$ will give us the cosmic time difference between t_0 (observer cosmic time) and t_e (the cosmic time in which the photon was emitted). If we integrate Eq. 1.24 to $z \to \infty$ we get the age of the universe. For the parameters given in 1.22 our Universe is $t_L \approx 13.8$ Gyr old [6]. Figure 1.3 shows the scale factor in terms of redshift and lookback time annotating some relavant cosmic events.

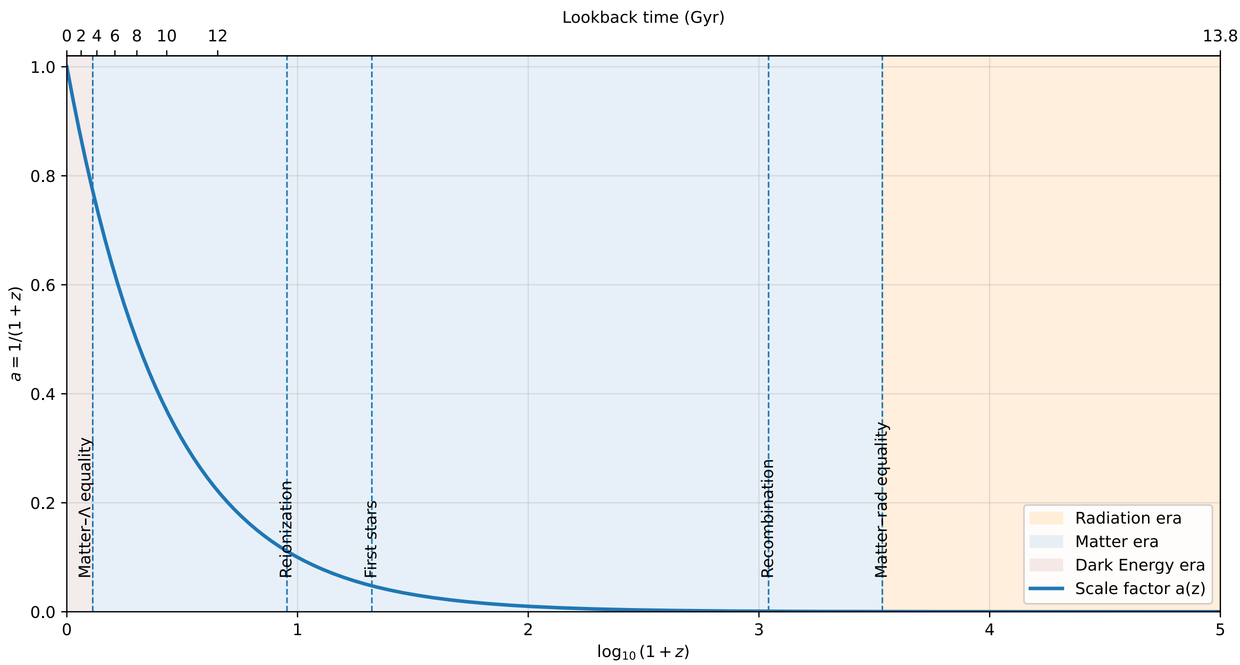

Figure 1.3: Scale factor $a = 1/(1+z)$ as a function of $\log_{10}(1+z)$ for the parameter in 1.22. The top axis shows the corresponding lookback time in Gyr, computed by numerical integration of Eq. 1.24. Shaded regions indicate the radiation-dominated, matter-dominated, and dark-energy-dominated eras. Vertical dashed lines mark key transitions [6]: recombination ($z \approx 1100$), first-star era ($z \approx 20$), reionization ($z \approx 6$–8), matter–radiation equality ($z \approx 3400$), and matter–Λ equality ($z \approx 0.30$).

The set of assumptions that compose the ΛCDM model together with the observational parameters are enough to describe a wide range of phenomena with great accuracy, such as [9]: the angular distribution of the CMB, baryon acoustic osculations features of the primordial plasma in CMB, the abundance of deutherion from nucleosynthesis, the statistics of weak gravitational lensing, etc. The ΛCDM model is the current standard for cosmology, and is the benchmark against which any new physics should be compared to.

1.4 Challenges of the ΛCDM model

Despite its success, the ΛCDM model has its theoretical and observational challenges, hinting at extensions or modifications [6]. Firstly, listing some main theoretical ones:

1. **Origin of the primordial perturbations:** The universe is highly homogeneous and isotropic. Random stochastic perturbations to this field are not enough to account for the formation of structure as we observe.

2. **Flatness Problem:** Observations indicate that the Universe is very close to $k = 0$, meaning it was exceptionally flat in the early Universe, where small deviations would be greatly amplified by expansion.

3. **Horizon Problem:** The temperature in the CMB appears highly homogeneous and isotropic, but the expansion rate would not allow different regions of the universe to interact causally to achieve thermal equilibrium.

4. **Singularity Problem:** The GR solution predicts a point of zero volume and infinite energy at the Big Bang, indicating a breakdown of our current understanding of gravitation.

5. **Nature of Dark Energy:** Observations of Type Ia supernovae indicate that the expansion of the Universe is accelerating, which cannot be explained by current matter or radiation components. Vacuum energy from Quantum Field Theory (QFT) predicts values 120 orders of magnitude higher than that of Λ in cosmology.

6. **Nature of Dark Matter:** Without CDM the model cannot predict the formation of structure as early as observed, but despite having a framework of how CDM interacts, we do not know its intrinsic nature.

Points 1, 2 and 3 require a great deal of fine tuning to the initial conditions to reproduce our observational results. Inflationary theory addresses these points giving a causal physical origin to them [6]. It proposes a period of rapid expansion at the early universe driven by a scalar field denominated Inflaton. This period lasted around 10^{-35} s, but was enough to achieve a couple things: it erases classical inhomogeneities and curvature leading to a flat universe, it stretches the different regions of the Universe from a time they were causally connected, and finally, quantum fluctuations in the Inflaton field were stretched to cosmological scales, causing the gaussian random field that is the seed of structure in the Universe.

It is important to point out that inflation comes with its own set of theoretical problems, and although it justifies some observational measurements, the exact nature of the Inflaton field is unknown, and we have not found a way to observationally probe the early Universe in its earliest, which is where inflation took place, so the problems remain open for investigation [6].

Problem 4, the singularity [10], persists even within inflationary frameworks. One school of thought admits that the Big Bang singularity may not have existed at all. Instead, the Universe could have undergone a prior contraction phase that was reversed by repulsive quantum gravitational effects, leading to a “bounce” into expansion [11]. Researchers are exploring this problem through modified gravity theories, semi-classical and fully quantum gravitational approaches [12]. Resolving this issue requires a theory of gravitation that remains consistent at quantum mechanical scales, one of the greatest challenges in cosmology and physics as a whole.

In Problem 5 the simple parametrization of Λ as a uniform energy density that permeates space and exerts negative pressure is enough to provide agreement with observational data such as Type Ia supernovae and CMB anisotropies. However, recent DESI DR2 baryon acoustic oscillation (BAO) results have added an important nuance: although the BAO measurements themselves are still well described by flat ΛCDM, their combination with CMB and Type Ia supernova data shows a preference for a time-evolving dark-energy equation of state over a strict cosmological constant [13, 14]. Questions still remain; some believe that the origin of Λ is the zero-point energy predicted by QFT, although current theoretical predictions do not match [15]. Researchers seek out extensions or modifications of both GR and QFT, and even philosophical approaches, like the anthropic principle, to describe this phenomenon. Problem 6, the nature of dark matter, faces similar challenges and will be discussed in more detail in the next section.

Observationally the ΛCDM faces increasing scrutiny from high precision measurements of its parameters, and we have subtle but persistent tensions between different sources. The most notable is the Hubble tension, where Hubble parameter found by the Planck collaboration via the CMB analysis is [9]

$$H_0^{\text{Planck}} = 67.4 \pm 0.5 \ \mathrm{km\,s^{-1}\,Mpc^{-1}}$$

And the local Cepheid-calibrated Type Ia supernova predicts the significantly higher value of

$$H_0^{\text{local}} \approx 73.0 \ \mathrm{km\,s^{-1}\,Mpc^{-1}}\,.$$

Another tension related to the growth of structure exists, the S_8 tension, which will be discussed in the coming sections. These tensions may indicate unaccounted systematic uncertainties in data or analysis pipelines, but they could also signal the limits of the ΛCDM paradigm itself, hinting at new physics. Future surveys are planned to produce extraordinary amount of cosmological data, that is why modeling and computational tools should be up to date to not introduce systematic errors to the results.

2 STRUCTURE AND DARK MATTER HALOS

All the development written until here gave a general overview of the current state of cosmology. In this section we will expand the details for the most important part for this work: Large Scale Structure (LSS). How matter evolved to form the intricate cosmic web we see today, and how the study of this LSS leads to basic cosmological parameters.

2.1 Dark Matter

Dark matter (DM) is postulated in order to account for gravitational effects observed in very large scale structures (the "non-keplerian" rotation curves of galaxies, the gravitational lensing of light by galaxy clusters, and the enhanced clustering of galaxies) that cannot be accounted for by the quantity of observed matter. As for the parameters described in 1.22, dark matter accounts roughly for 26% of the Universe energy budget. The ΛCDM model proposes specifically cold dark matter, hypothesized as [16]:

- Non-baryonic: Consists of matter other than protons and neutrons (and electrons, by convention, although electrons are not baryons)
- Cold: Its velocity is far less than the speed of light at the epoch of radiation-matter equality (thus neutrinos are excluded, being non-baryonic but not cold)
- Dissipationless: Cannot cool by radiating photons
- Collisionless: Dark matter interact only through gravity

Although this definitions is sufficient to account for all cosmological phenomenons, the intrinsic nature of dark matter is an ongoing debate. From theory, several classes of DM candidates were proposed [16]:

- Weakly Interacting Massive Particles (WIMPs): An extension of the standard model of physics, adds heavy particles that interact only through gravity and the weak force, expected to have been produced thermally in the early Universe.
- Axions: Very light particles originally proposed to solve a problem in the theory of strong interactions, they can form a cold and smooth background field that clumps under gravity, acting as dark matter on large scales.
- Primordial Black Holes: Small black holes formed in the early Universe by tightly packed subatomic matter.
- Modified Gravity: Changes to gravity laws themselves that reproduce dark matter effects.

Other possibilities discussed in the literature include fuzzy dark matter, usually modeled as an ultralight bosonic field with astrophysically relevant wave effects, and fermionic dark matter, often explored in scenarios involving sterile neutrinos or self-gravitating neutral fermions [17–19].

Whichever it is or is not, none of them have any observational evidence from astrophysics or collision particle physics as of yet, but the scenario is favorable for a particle-like DM.

As discussed in the last section, Cold Dark Matter provided the scaffolding in which baryons would later accrete to form the luminous structures we observe today. The cold and collisionless nature of dark matter ensures that small-scale perturbations survive and grow hierarchically: small overdense regions form first and merge to progressively create larger systems. These collapsed overdense regions form gravitationally bound objects decoupled from cosmic expansion, known as Dark Matter Halos, the building blocks of structure. These can be as small as the Earth or the Moon (depending on the DM model used) to the top of the hierarchy covering several Megaparsecs, the Galaxy Clusters [16].

2.2 Linear Regime

For instances where the density contrast $|\delta| \ll 1$ we can describe the matter density field by the framework given in Section 1.2 [6]. Firstly, we want to find the matter power spectrum from the correlation function Eq. 1.20

$$\langle \delta(\boldsymbol{k})\, \delta^*(\boldsymbol{k}') \rangle = (2\pi)^3 \delta_D(\boldsymbol{k} - \boldsymbol{k}')\, \mathcal{P}(k), \tag{2.1}$$

we also introduce the dimensionless form of the power spectrum

$$\Delta^2(k) \equiv \frac{k^3 \mathcal{P}(k)}{2\pi^2}. \tag{2.2}$$

An useful measure is the root-mean-square of linear matter fluctuations smoothed with top-hat filter of radius R, representing a sphere in real space, defined as [20]

$$\begin{aligned} \sigma^2(R) &= \int_0^\infty \frac{\mathrm{d}k}{k} \frac{k^3}{2\pi^2} \mathcal{P}(k)\, |W(kR)|^2 \\ \sigma^2(R) &= \int_{-\infty}^\infty \mathrm{d}\ln k\, \Delta^2(k)\, |W(kR)|^2. \end{aligned} \tag{2.3}$$

The top-hat function is defined in Fourier space as

$$W(kR) = \frac{3}{(kR)^3} (\sin(kR) - kR\cos(kR)). \tag{2.4}$$

Is of importance to note that the mass enclosed by the sphere, where $\bar{\rho}$ is the mean density of the region will be

$$M = \frac{4}{3} \pi R^3 \bar{\rho}. \tag{2.5}$$

$\sigma^2(R)$ measures the "clumpiness" of matter on spheres of radius R. A common choice for R is $8h^{-1}\,\mathrm{Mpc}$ [20], and another dependency we have been omitting is that the contrast $\delta(\boldsymbol{x}, t)$ depends on cosmic time as well, but this can easily be written in terms of redshift $\delta(\boldsymbol{x}, z)$. We define then another cosmological parameter, σ_8 which is Eq. 2.3 taken for $R = 8h^{-1}, \mathrm{Mpc}$ at $z = 0$.

A related cosmological parameter is S_8

$$S_8 \equiv \sigma_8 \sqrt{\frac{\Omega_m}{0.3}} \tag{2.6}$$

it is a degenerate combination of σ_8 and Ω_m. The parameters σ_8 and S_8 thus summarize the present-day amplitude of matter clustering on the linear regime and provide key observational constraints on the growth of structure.

2.3 Non Linear Regime

In the linear regime perturbations evolve independently and the power spectrum fully describes their statistics. On smaller scales, where overdensities become significant ($\delta \gtrsim 1$), the evolution departs from linear theory, leading to mode coupling, collapse, and the formation of bound dark matter halos [6].

The non-linear regime is not trivial and no analytical solution is available, but a simplified and highly symmetrical approximation, the spherical collapse model, can capture some physical definitions. We will follow the evolution of a single spherical overdense region evolving in a homogeneous and isotropic background. Its dynamics can be described by a Friedmann equation:

$$\left(\frac{\dot{R}}{R}\right)^2 = \frac{8\pi G}{3}\rho_{\text{int}} - \frac{k}{R^2}, \tag{2.7}$$

where $R(t)$ is the physical radius of the spherical perturbation, ρ_{int} its internal matter density, and $k > 0$ an effective curvature parameter arising from the initial overdensity.

At early times, $R(t) \propto a(t)$ and the region expands with the Universe. As the self-gravity of the perturbation becomes dominant, the expansion decelerates until $\dot{R} = 0$ at a turnaround point ($t = t_{\text{ta}}$). From Eq. (2.7), this condition implies:

$$\frac{8\pi G}{3}\rho_{\text{int}}(t_{\text{ta}}) = \frac{k}{R_{\text{ta}}^2}. \tag{2.8}$$

The Friedmann equations for a closed Universe can be writen in parametric form [6]:

$$R(\theta) = A(1 - \cos\theta), \tag{2.9}$$

$$t(\theta) = B(\theta - \sin\theta), \tag{2.10}$$

Here θ is a development angle running from 0 to 2π, the perturbation starts expanding ($R = 0$, $\theta = 0$), halts ($R = R(t_a)$, $\theta = \pi$), and collpses ($R = 0$, $\theta = 2\pi$). Here A and B are integration constants that set the characteristic length and time scales of the bound perturbation. In particular, they may be written as $A = GM/k$ and $B = GM/k^{3/2}$, so that $R_{\rm ta} = 2A$ and $t_{\rm ta} = \pi B$.

The turnaround time and radius are:

$$R_{\rm ta} = A(1 - \cos\pi) = 2A, \quad t_{\rm ta} = B(\pi - \sin\pi) = \pi B. \tag{2.11}$$

The density of the perturbation and of the background evolve as

$$\rho(\theta) = \frac{M}{(4\pi/3)r^3(\theta)} = \frac{3M}{4\pi A^3}\frac{1}{(1-\cos\theta)^3}, \tag{2.12}$$

$$\bar{\rho}(\theta) = \frac{1}{6\pi G t^2(\theta)} = \frac{1}{6\pi G B^2}\frac{1}{(\theta-\sin\theta)^2}. \tag{2.13}$$

The ratio of Eq. 2.12 and Eq. 2.13 determines the density contrast

$$1 + \delta = \frac{\rho}{\bar{\rho}} = \frac{9}{2}\frac{(\theta-\sin\theta)^2}{(1-\cos\theta)^3}. \tag{2.14}$$

At turnaround, the density contrast is

$$\delta_{ta} = \frac{9\pi^2}{16} - 1 \simeq 4.55, \tag{2.15}$$

From here we can also set a upper bound to linear perturbations before they become non linear. This is done by taking the first order approximation of 2.14 [6, 20]

$$\delta_c \equiv \delta_{\rm lin}(t_{\rm col}) = \frac{3}{20}(12\pi)^{2/3} \simeq 1.686. \tag{2.16}$$

After turnaround, the region begins to collapse. In a purely pressureless system, this collapse would lead to a singularity at $\theta = 2\pi$. However, in reality, the system reaches equilibrium. As the collapsing region contracts beyond turnaround, random motions of its constituent particles grow due to gravitational interactions. Eventually, these motions establish a state of dynamical equilibrium, in which the system's average kinetic and potential energies become related through the virial theorem. This theorem, derived from the average over time of the total kinetic energy of a stable system of discrete particles bound by a conservative force, states that for a stable configuration held together by gravity [6]

$$2T + U = 0, \tag{2.17}$$

where T is the total kinetic energy and U is the total potential energy. The gravitationally bound object left after non linear collapse reaches virialization is the Dark Matter Halo.

At turnaround, the kinetic energy vanishes ($T_{\rm ta} = 0$), so the total energy E is purely potential:

$$E = U_{\rm ta} = -\frac{3GM^2}{5R_{\rm ta}}. \tag{2.18}$$

At virialization (t_{vir}), the total energy must remain conserved:

$$E = T_{\text{vir}} + U_{\text{vir}} = \frac{1}{2} U_{\text{vir}}. \tag{2.19}$$

Equating these gives:

$$U_{\text{vir}} = 2U_{\text{ta}} \quad \Rightarrow \quad R_{\text{vir}} = \frac{1}{2} R_{\text{ta}}. \tag{2.20}$$

Hence, the virial radius is half the turnaround radius $r_{\text{vir}} = r_{ta}/2$, and eight times the density at turnaround $\rho_{\text{vir}} = 9\rho_{ta}$. Combining with the background evolution, we find that at the virialization time [6, 20]

$$\frac{\rho_{\text{int}}(t_{\text{vir}})}{\bar{\rho}(t_{\text{vir}})} = 18\pi^2 \simeq 178 \tag{2.21}$$

for an Einstein-de Sitter universe. This is the canonical virial overdensity Δ_{vir} often used to define dark matter halos in simulations

$$\rho_{\text{halo}} = \Delta_{\text{vir}} \rho_c(z) \tag{2.22}$$

In ΛCDM cosmologies, Δ_{vir} depends slightly on redshift and cosmological parameters, typically ~ 200 at $z = 0$ [6, 20].

2.4 Halo Mass Function

The spherical collapse analytical model is highly limited and cannot address situations of multiple overdensities evolving. In the non-linear regime, the matter distribution can be described statistically as a collection of dark matter halos, each containing mass distributed according to some density profile. The halo model assumes that all matter in the Universe is bound within these halos, and the clustering of matter arises from correlations both within and between them.

Spherical collapse gives us a good start developing a full halo theory. The Press-Schechter formalism [21] provides an analytic framework to predict the halo mass function, the comoving number density of halos per unit mass interval, by realizing that the linear regime can be mapped to the non linear regime through densities in the linear density exceeding a critical density, the one found in the spherical collapse model (Eq. 2.16) δ_c is constant, though in the ΛCDM case there is slight redshift dependency $\delta_c(z)$.

We first introduce the dimensionless parameter ν, called peak height:

$$\nu = \frac{\delta_c(z)}{\sigma(M, z)}, \tag{2.23}$$

where $\sigma^2(M)$ is computed in the linear matter power spectrum with Eq. 2.3 for a radius encompassing the mass M. This parameter thus measures the significance of a fluctuation relative to the typical background variance.

The comoving number density of halos is given by [6]

$$\frac{dn}{dM} = \frac{\bar{\rho}_m}{M} f(\nu) \frac{d\nu}{dM}, \tag{2.24}$$

here $f(\nu)$ is the multiplicity function derived from gaussian initial conditions:

$$f(\nu) = \sqrt{\frac{2}{\pi}}\, \nu \, \exp[-\nu^2/2] \,. \tag{2.25}$$

The derivative of peak height in Eq. 2.24 is

$$\frac{d\nu}{dM} = -\frac{\delta_c}{\sigma^2} \frac{d\sigma}{dM} \tag{2.26}$$

The final form is known as the Halo Mass Function [6]

$$\frac{dn}{dM}(M,z) = \sqrt{\frac{2}{\pi}}\, \frac{\bar{\rho}_m}{M^2}\, \frac{\delta_c(z)}{\sigma(M,z)} \left| \frac{d\ln\sigma(M,z)}{d\ln M} \right| \exp\left[-\frac{\delta_c^2(z)}{2\,\sigma^2(M,z)} \right], \tag{2.27}$$

which quantifies how many dark matter halos of a given mass exist per unit comoving volume. While the Press-Schechter formulation captures the general behavior, it systematically underpredicts low-mass halos and overpredicts high-mass ones due to its simplifying assumptions (like spherical collapse, sharp mass threshold, etc). Improved empirical fits such as the Sheth-Tormen, Jenkins, and Tinker mass functions incorporate ellipsoidal collapse and results from N-body simulations, offering better agreement with numerical data across redshifts and cosmologies [6].

2.5 Halo Bias

The mass function informs how many halos of a given mass we should find in a given volume. The next step is to determine how the halos are distributed in this volume. This is done by computing the correlation between halo positions, and how they interact with the underlying matter density field. We define the halo density contrast as

$$\delta_h(\boldsymbol{x}; M) \equiv \frac{n(\boldsymbol{x}; M) - \bar{n}(M)}{\bar{n}(M)} \tag{2.28}$$

similar to the density contrast of matter, for halos define the over or under densities of haloes of mass M at position $\boldsymbol{x}$, compared to the mean in the entire region $\bar{n}(M)$. From the halo density contrast we can also define the two point correlation function, or "halo-halo" correlation function

$$\xi_{hh}(r; M) = \langle \delta_h(\boldsymbol{x}; M)\, \delta_h(\boldsymbol{x} + \boldsymbol{r}; M) \rangle. \tag{2.29}$$

A common aproach to tackle this problem is the technique called "peak background split" [6], where we separate the density perturbation into a short wavelength part, representing the peaks δ_h, and a long wavelenght part, representing the background contrast δ_b. So the total contrast is

$$\delta = \delta_h + \delta_b, \tag{2.30}$$

where, by definition, $\delta_b \ll 1$ and can be treated in the linear regime. Assuming the dependence of the halo density field to the background, we can expand the halo mass function to first order in δ_b

$$\begin{aligned}\frac{dn_h}{dM}(\delta_b) &= \frac{d\bar{n}_h}{dM} + \left[\frac{\partial}{\partial\bar{\rho}'}\left(\frac{d\bar{n}_h}{dM}\right)\frac{d\bar{\rho}'}{d\delta_b} + \frac{\partial}{\partial\delta_c'}\left(\frac{d\bar{n}_h}{dM}\right)\frac{d\delta_c'}{d\delta_b}\right]\delta_b \\ &= \frac{d\bar{n}_h}{dM}\left[1 + \left(\bar{\rho}\frac{\partial}{\partial\bar{\rho}'}\ln\left(\frac{d\bar{n}_h}{dM}\right) - \frac{\partial}{\partial\delta_c'}\ln\left(\frac{d\bar{n}_h}{dM}\right)\right)\delta_b\right].\end{aligned} \tag{2.31}$$

Although the algebra is convoluted, using the definition for the halo mass function Eq. 2.27, we can reduce Eq.2.31 to

$$\frac{dn_h}{dM}(\delta_b) = \frac{d\bar{n}_h}{dM}\left[1 + \left(1 + \frac{\nu^2 - 1}{\delta_c}\right)\delta_b\right], \tag{2.32}$$

the contrast in Eq. 2.28 can then be written as

$$\delta_h(\boldsymbol{x}; M) = \left(1 + \frac{\nu^2 - 1}{\delta_c}\right)\delta_b(\boldsymbol{x}). \tag{2.33}$$

The factor relating δ_h and δ_b is the linear halo bias

$$b(\nu) = 1 + \frac{\nu^2 - 1}{\delta_c}. \tag{2.34}$$

Figure 2.1 shows a schematic plot illustrating how the the formation of halos is biased by the background matter distribution.

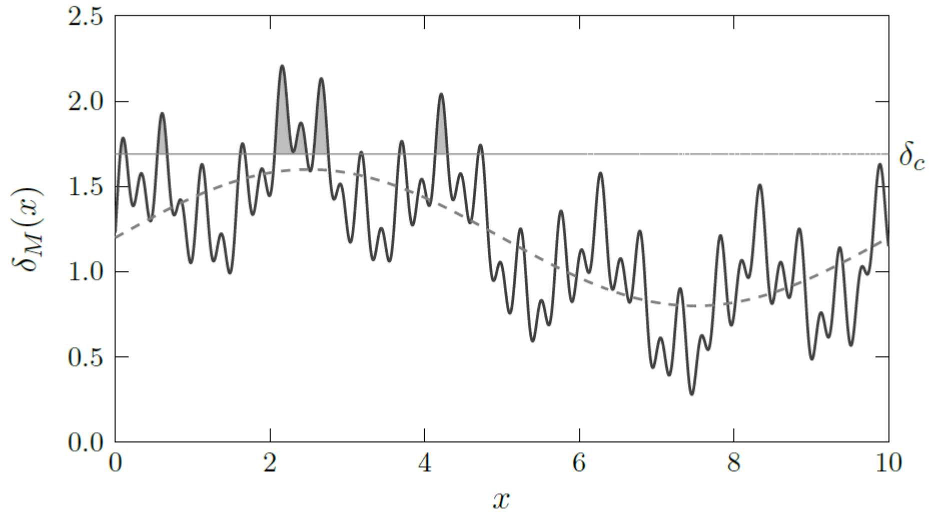

Figure 2.1: Schematic illustration of the peak-background split. The solid black line represents the total matter density contrast $\delta_M(x)$, which can be decomposed into a long-wavelength background mode (dashed line) and short-wavelength fluctuations. Halo formation occurs where the total density contrast exceeds the critical threshold δ_c, and the presence of a positive background fluctuation δ_b increases the likelihood of reaching this threshold. Source: Figure 5.7 in [6].

Now the halo correlation function Eq. 2.29 can be related to the linear correlation function

$$\xi_{hh}(r; M) = b^2(M)\xi_{lin}(r). \tag{2.35}$$

The bias described here comes from the Press-Schechter definition of the halo mass function, other definition result in modified biases. Generally the bias is the ratio of the halo and linear matter power spectra [22]

$$b \equiv \sqrt{\frac{\mathcal{P}_h(k)}{\mathcal{P}_{lin}(k)}}. \tag{2.36}$$

2.6 Halo Correlations

Until here we defined two correlation functions: ξ_{hh} "halo-halo" and ξ_{lin}, also called "matter-matter" ξ_{mm} . Another useful correlation is the "halo-matter" correlation function, relating halo centers to the matter density field. The correlation ξ_{hm} is then defined with the matter contrast δ_m (Eq. 1.16) and the halo contrast δ_h (Eq. 2.28)

$$\xi_{hm}(r) = \langle \delta_h(\boldsymbol{x})\, \delta_m(\boldsymbol{x} + \boldsymbol{r}) \rangle. \tag{2.37}$$

Using the contrast definition we can arrive at [23]

$$\xi_{hm}(r) = \frac{\langle \rho(r) \rangle - \bar{\rho}}{\bar{\rho}}, \tag{2.38}$$

where $\langle\rho(r)\rangle$ is the density of the halo at radius r averaged by all halos in the sample.

ξ_{hm} can be separated into two regimes, one where the correlation is dominated by particles inside the halo, and another where it is dominated by particles inside other halos, respectively called one-halo ξ_{1h} and two-halo ξ_{2h} terms. For large scales the two-halo term follows [23]

$$\xi_{2h} = b(M)\xi_{lin}, \tag{2.39}$$

offset by a factor of b compared to the halo-halo correlation. Whereas the one-halo term is defined as [23]

$$\xi_{1h} = \frac{\rho(r;M) - \bar{\rho}_m}{\bar{\rho}_m}. \tag{2.40}$$

The term $\rho(r;M)$ is the Halo Density Profile, it describe how matter is distributed inside the halo, and is the main object of interest of this work that will be discussed extensively in the next Chapter. It is not only important for correlation, but also to model a variety of astrophysical phenomena, and can be related to structure and cosmological parameters. As we will see, no analytical solution exist for this profile, and we heavily rely on simulations.

To close this Chapter, as it could not put it in better words, a direct quote the extremely useful review on the Halo Model [20]:

> The halo properties that are required to make a prediction using the halo model are the halo bias (how haloes cluster relative to matter), halo mass function (number density of haloes with different masses), and halo profile (how matter or its tracers are distributed within a halo). These ingredients are most often extracted from numerical simulations and (sometimes) calibrated across a range of cosmological parameters. It is usual to assume that haloes are linearly biased, spherical objects with properties that are only a function of the halo mass, although these restrictions can be relaxed.

3 WEAK GRAVITATIONAL LENSING

General Relativity predicts that the presence of matter can deflect the path of light rays traveling across it, because of the curvature this mass generates into spacetime, light taking geodesic paths will appear bent [5]. In the astrophysical context, light from a distant source deflected by a matter distribution (such as galaxies and galaxies clusters) on its way to an observer is called gravitational lensing. Lensing properties are sensitive to the full matter content, both baryonic and non baryonic, giving us a special probe of the structure of dark matter halos, and as we will see, the large scale structure of the Universe.

The effect of this lens can be enough to create optical artifacts, like multiple images, arcs or rings to the image that reaches the observer, this regime is called strong lensing (Fig. 3.1 shows examples) [24]. In most cases these deflections are small, this regime is called weak lensing (WL), producing the percent level magnification and distortion effects. The study of WL is statistical in nature because these small perturbations to the shape observed need to be taken for an ensemble of objects distorted by the lens [24].

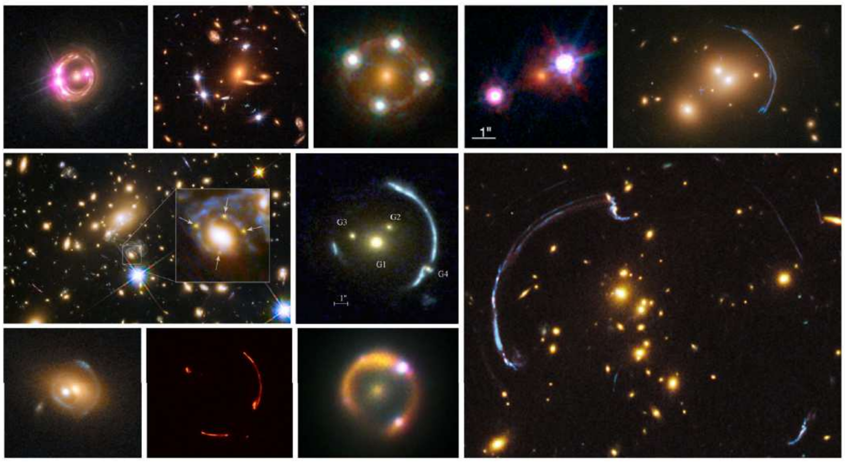

Figure 3.1: Various strong lens systems detected by the Hubble Space Telescope, the most dramatic are the called Einstein Rings and Einstein Crosses. Source: Figure 1 in [25]

3.1 Lens Equation

We begin our modeling of the gravitational lens observing the sketch of a typical lens in Fig. 3.2:

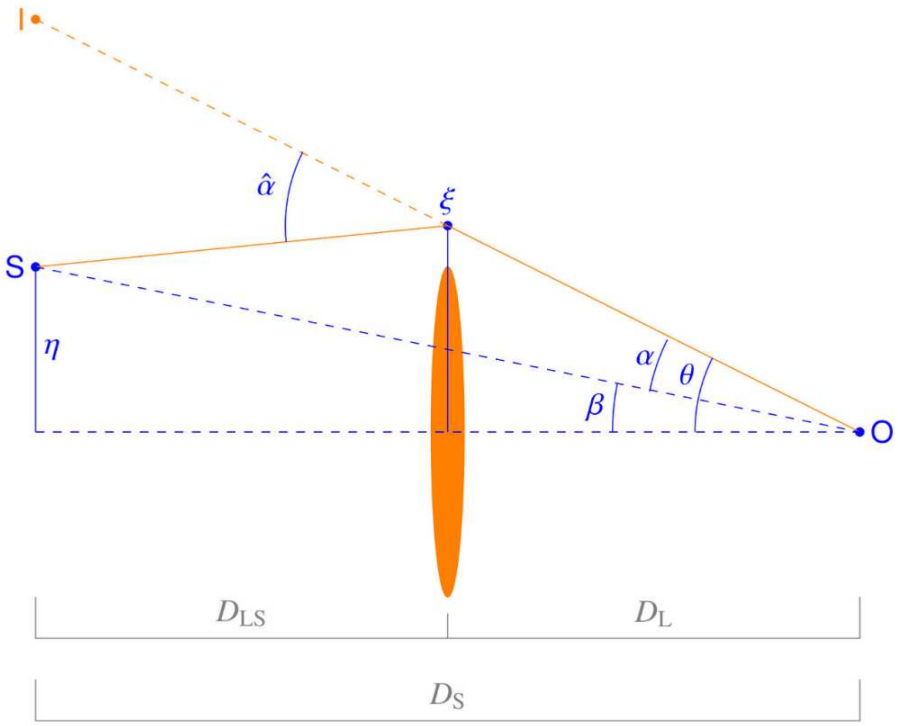

Figure 3.2: Sketch of a gravitational-lens system. Source: Figure 1 in [26].

In this scenario, a mass concentration sits at an angular diameter distance D_{LS} deflecting light rays coming from a source at D_S, if the extent of the deflecting mass is much smaller than the observer-lens-source separation we have the called thin lens approximation. A famous result from GR [27] is the prediction of the deflection angle of a light ray passing by a point mass, in the limit where the parameter ξ is much larger than the Schwarzschild Radius ($\xi \gg R_s \equiv 2GM\,c^{-2}$) [26]

$$\hat{\alpha} = \frac{4GM}{c^2\xi}, \tag{3.1}$$

this is twice os what the Newtonian theory predicts, and was one of the early experimental results of GR. For a distribution with density profile $\rho(\boldsymbol{r})$, we have the volume elements

$$\mathrm{d}m = \rho(\boldsymbol{r})\,\mathrm{d}V, \tag{3.2}$$

and we also define the light ray trajectory to be

$$(\xi_1(\lambda), \xi_2(\lambda), r_3(\lambda)), \tag{3.3}$$

here, λ means a parameter along the light ray trajectory, where the coordinates are chosen so that the light ray propagates along the incoming direction r_3. If the deflection angle is small enough, in the neighborhood of the deflecting mass, it can be approximated to be straight. This is the Born approximation used in atomic nuclear physics. In this scenario, the trajectory is [24]

$$\boldsymbol{\xi}(\lambda) \approx \boldsymbol{\xi} = \text{const.} \tag{3.4}$$

The impact vector of a light ray relative to a mass element $\mathrm{d}m$ at $\xi' = (\xi'_1, \xi'_2, r'_3)$ is then $\boldsymbol{\xi} - \boldsymbol{\xi}'$, independent of r'_3. In weak field limit of GR, where the metric can be linearized, the contributions of each mass element to the deflection stack linearly, and the total angle of the deflection α is [24]

$$\hat{\alpha}(\boldsymbol{\xi}) = \frac{4G}{c^2} \sum dm(\xi'_1, \xi'_2, r'_3) \, \frac{\boldsymbol{\xi} - \boldsymbol{\xi}'}{|\boldsymbol{\xi} - \boldsymbol{\xi}'|^2} \tag{3.5}$$

$$= \frac{4G}{c^2} \int d^2\xi' \int dr'_3 \, \rho(\xi'_1, \xi'_2, r'_3) \, \frac{\boldsymbol{\xi} - \boldsymbol{\xi}'}{|\boldsymbol{\xi} - \boldsymbol{\xi}'|^2}. \tag{3.6}$$

Here we can recognize the surface mass density, which is the mass density projected onto a plane perpendicular to the incoming light ray

$$\Sigma(\boldsymbol{\xi}) \equiv \int \mathrm{d}r_3 \, \rho(\xi_1, \xi_2, r_3), \tag{3.7}$$

the angle becomes

$$\hat{\alpha}(\vec{\xi}) = \frac{4G}{c^2} \int d^2\xi' \, \Sigma(\boldsymbol{\xi}') \, \frac{\boldsymbol{\xi} - \boldsymbol{\xi}'}{|\boldsymbol{\xi} - \boldsymbol{\xi}'|^2}. \tag{3.8}$$

We now need to relate the true position of the source to the observed position in the sky. Reading the trigonometry of Fig. 3.2 we have the relation, with the angular coordinates $\boldsymbol{\eta} = D_s \boldsymbol{\beta}$ and $\boldsymbol{\xi} = D_d \boldsymbol{\theta}$

$$\boldsymbol{\beta} = \boldsymbol{\theta} - \frac{D_{LS}}{D_S} \hat{\boldsymbol{\alpha}}(D_L \boldsymbol{\theta}) \equiv \boldsymbol{\theta} - \boldsymbol{\alpha}(\boldsymbol{\theta}), \tag{3.9}$$

where in the last step the scaled deflection angle $\boldsymbol{\alpha}(\boldsymbol{\theta})$ is defined. Equations 3.8 and 3.9 tell us that a source at $\boldsymbol{\beta}$ will be seen at $\boldsymbol{\theta}$, with possibly multiple solutions of $\boldsymbol{\theta}$ generating multiple images. We can use this aspect to formally define the difference between weak and strong lensing. What quantifies this is the dimensionless surface mass density, or convergence $\kappa(\boldsymbol{\theta})$ [24]

$$\kappa(\boldsymbol{\theta}) = \frac{\Sigma(D_d \boldsymbol{\theta})}{\Sigma_c}, \quad \Sigma_c = \frac{c^2}{4\pi G} \frac{D_S}{D_L D_{LS}}. \tag{3.10}$$

Σ_c is the critical surface mass density, it defines the threshold in each multiple images can occur. Regions with $\kappa \geq 1$ are strong enough to produce multiple images for symmetrical lenses. In terms of κ, the scaled deflection angle is

$$\boldsymbol{\alpha}(\boldsymbol{\theta}) = \frac{1}{\pi} \int \mathrm{d}^2\theta' \, \kappa(\theta') \frac{\boldsymbol{\theta} - \boldsymbol{\theta}'}{|\boldsymbol{\theta} - \boldsymbol{\theta}'|^2}. \tag{3.11}$$

The deflection angle can also be written in terms of a deflection potential

$$\boldsymbol{\alpha}(\boldsymbol{\theta}) = \nabla\psi_\theta(\boldsymbol{\theta}). \tag{3.12}$$

This is the analogous of the Newtonian gravitational potential in two dimensions. The Poisson equation reads [26]

$$\nabla^2\psi(\boldsymbol{\theta}) = \frac{8\pi G}{c^2}\frac{D_L D_{LS}}{D_S}\Sigma = 2\kappa(\boldsymbol{\theta}), \tag{3.13}$$

and Eq. 3.11 can also be expressed in terms of the potential

$$\psi(\boldsymbol{\theta}) = \frac{1}{\pi}\int \mathrm{d}^2\theta'\,\kappa(\theta')\,\ln|\boldsymbol{\theta} - \boldsymbol{\theta}'|^2. \tag{3.14}$$

3.2 Shear, Convergence and Magnification

Weak lensing does not only alter the apparent position of a source, it also distorts its observed shape and changes its flux. These effects arise because the mapping between the source plane and the image plane is not one-to-one but varies across angles on the sky.

We consider a small perturbation $\delta\boldsymbol{\theta}$ in the image plane. The corresponding change in the source position is obtained by linearizing the mapping:

$$\delta\boldsymbol{\beta} = \boldsymbol{A}(\boldsymbol{\theta})\,\delta\boldsymbol{\theta}, \tag{3.15}$$

where the Jacobian Matrix of the lens mapping is defined as

$$\boldsymbol{A}(\boldsymbol{\theta}) \equiv \frac{\partial\boldsymbol{\beta}}{\partial\boldsymbol{\theta}} = \boldsymbol{I} - \frac{\partial\boldsymbol{\alpha}}{\partial\boldsymbol{\theta}}. \tag{3.16}$$

From the deflection potential (Eq. 3.14), the Jacobian decomposes naturally into second derivatives [24]

$$\boldsymbol{A} = \left(\delta_{ij} - \frac{\partial^2\psi(\boldsymbol{\theta})}{\partial\theta_i\partial\theta_j}\right) = \begin{pmatrix} 1-\psi_{,11} & -\psi_{,12} \\ -\psi_{,12} & 1-\psi_{,22} \end{pmatrix}, \tag{3.17}$$

where commas denote partial derivatives. It is customary to introduce the *convergence* and *shear components*:

$$\begin{aligned} \kappa &= \frac{1}{2}(\psi_{,11} + \psi_{,22}), \\ \gamma_1 &= \frac{1}{2}(\psi_{,11} - \psi_{,22}), \\ \gamma_2 &= \psi_{,12}, \end{aligned} \tag{3.18}$$

which separate the isotropic and anisotropic parts of the distortion. In terms of these fields, the

Jacobian becomes [26]

$$\boldsymbol{A} = \begin{pmatrix} 1-\kappa-\gamma_1 & -\gamma_2 \\ -\gamma_2 & 1-\kappa+\gamma_1 \end{pmatrix}. \tag{3.19}$$

The parameters κ, γ_1 and γ_2 form the fundamental lensing fields that describe how light bundles are distorted. The convergence κ produces an isotropic magnification of the image, increasing or decreasing its apparent size without changing its shape.

The components γ_1 and γ_2 combine into a complex shear

$$\gamma = \gamma_1 + i\,\gamma_2, \tag{3.20}$$

which stretches images along orthogonal axes. Shear does not alter the area of the image to first order, but changes its ellipticity. This quantity is central to weak lensing analyses: by statistically averaging galaxy ellipticities, the underlying shear field can be reconstructed. Observationally, the image we see is in the $\boldsymbol{\theta}$ plane, the transformation is then [26]

$$\delta\boldsymbol{\theta} = \boldsymbol{A}^{-1}\,\delta\boldsymbol{\beta}, \tag{3.21}$$

where the inverse Jacobian is solved as

$$\boldsymbol{A}^{-1} = \frac{1}{\det \boldsymbol{A}} \begin{pmatrix} 1-\kappa+\gamma_1 & \gamma_2 \\ \gamma_2 & 1-\kappa-\gamma_1 \end{pmatrix}. \tag{3.22}$$

The anisotropic part of this transformation is proportional to $\gamma/(1-\kappa)$ [24], so the measurable quantity is not the true shear γ, but the reduced shear

$$g(\boldsymbol{\theta}) = \frac{\gamma(\boldsymbol{\theta})}{1-\kappa(\boldsymbol{\theta})}, \tag{3.23}$$

because in practice we measure both κ and γ at the same time. In the weak lensing regime, where $|\kappa|, |\gamma| \ll 1$, we have $g \approx \gamma$ [26].

A derived quantity from κ and γ is the magnification μ, defined as the inverse of the determinant of the Jacobian

$$\mu(\boldsymbol{\theta}) = \frac{1}{\det \boldsymbol{A}} = \frac{1}{(1-\kappa)^2 - |\gamma|^2}. \tag{3.24}$$

Magnification changes the observed flux and number density of background sources. In the weak limit where $|\kappa|, |\gamma| \ll 1$, this reduces to

$$\mu \approx 1 + 2\kappa, \tag{3.25}$$

so that convergence dominates the magnification effect.

3.3 Cosmic Shear

In the last section we treated the deflection by a single overdensity source, but on cosmological scales light is deflected cumulatively as it travels through the inhomogeneous matter distribution of the Universe. This large scale manifestation of lensing is called cosmic shear. Cosmic shear measures the statistical contributions of all matter fluctuation, both dark and baryonic, integrated along the line of sight. The sensitivity to the full matter content makes it a prime probe of the large scale structure.

The firt step it to generalize the lensing potential in Eq. 3.14 to a extended lens. To do that we need to promote the distances of the thin lens to variables integrated along the line of sight. In a flat ΛCDM universe the comoving angular diameter distance is simply χ, the comoving radial coordinate. A point in the sky labeled by the angle $\boldsymbol{\theta}$ corresponds to the physical position $\boldsymbol{x}(\chi) = \chi\boldsymbol{\theta}$.

The angular diameter distances can be written in terms of the comoving radial coordinate [26]

$$D_d = a(\chi)\chi, \quad D_s = a(\chi_s)\chi_s, \quad D_{ds} = a(\chi_s)(\chi_s - \chi). \tag{3.26}$$

We will derive convergence for a extended lens, but this procedure can be used for the other functions like $\boldsymbol{\alpha(\theta)}$, $\psi(\boldsymbol{\theta})$, γ, etc. From de definition of κ in Eq. 3.10, the critical surface density Σ_c becomes

$$\Sigma_c = \frac{c^2}{4\pi G} \frac{a(\chi_s)\chi_s}{a(\chi)\,\chi\,(\chi_s - \chi)} \tag{3.27}$$

For the surface mass density, let $\rho(\chi, \theta)$ be the physical mass density along direction θ at distance χ. The differential contribution will be

$$\mathrm{d}\Sigma(\boldsymbol{\theta}, \chi) = \rho(\boldsymbol{\theta}, \chi)\, a(\chi)\, \mathrm{d}\chi \tag{3.28}$$

the correspondent convergence for this plane is then

$$\mathrm{d}\kappa(\boldsymbol{\theta}, \chi) = \frac{\mathrm{d}\Sigma(\boldsymbol{\theta}, \chi)}{\Sigma_c(\chi)} = \frac{4\pi G}{c^2} \frac{\chi(\chi_s - \chi)}{\chi_s}\, a^2(\chi)\, \rho(\boldsymbol{\theta}, \chi)\, d\chi, \tag{3.29}$$

integrating along the line of sight gives

$$\kappa(\theta, \chi) = \frac{4\pi G}{c^2} \int_0^{\chi_s} d\chi\, \frac{\chi(\chi_s - \chi)}{\chi_s}\, a^2(\chi)\, \rho(\theta, \chi). \tag{3.30}$$

It is also useful to write κ in terms of the density contrast, from the definition in Eq. 1.16

$$\rho(\boldsymbol{\theta}, \chi) = \bar{\rho}_m(\chi)[1 + \delta(\boldsymbol{\theta}, \chi)] \tag{3.31}$$

writing $\bar{\rho}_m$ in terms of the matter critical density (Eq. 1.12), we have

$$\bar{\rho} = \frac{3H_0^2}{8\pi G}\Omega_m a^{-3}. \tag{3.32}$$

The convergence in terms of the density contrast then becomes

$$\kappa(\theta) = \int_0^{\chi_s} d\chi\, W(\chi)\, \delta(\theta, \chi), \tag{3.33}$$

where we defined the weight function

$$W(\chi) = \frac{3H_0^2\Omega_m}{2c^2}\frac{\chi(\chi_s - \chi)}{\chi_s a(\chi)}. \tag{3.34}$$

This makes explicit that convergence is a weighted projection of the matter overdensity along the line of sight [26]. This cannot be predicted because the actual matter distribution in a particular line of sight is unknown, but we can access how lensing measurements correlate in space using two point statistics. For convergence we have, in real space

$$\xi_\kappa = \langle \kappa(\boldsymbol{\theta})\, \kappa(\boldsymbol{\theta}') \rangle. \tag{3.35}$$

Analogous to Eq. 1.20, we take this to Fourier space [26]

$$\langle \kappa(\boldsymbol{\ell})\, \kappa^*(\boldsymbol{\ell}') \rangle = (2\pi)^3 \delta_D(\boldsymbol{\ell} - \boldsymbol{\ell}')\, C_\ell^{\kappa\kappa}, \tag{3.36}$$

where $C_\ell^{\kappa\kappa}$ is the angular power spectrum. The difference here is that since convergence is a projected 2D field, we are using the 2D Fourier transformation with the angular scale ℓ. An implicit approximation here is to assume we are dealing we a patch of sky small enough to be considered flat, a treatment of the full sky needs a decomposition into spherical harmonics [26].

To relate to the full expression of convergence Eq. 3.33, we need to invoke the Limber's approximation that relates a projected angular power spectrum to the 3D power spectrum it is projected from. Conceptually what it does is: in a projected field, only structures at the same distance along the line of sight contribute to correlations, so the 3D power spectrum can be evaluated at transverse modes only, turning a hard 3D correlation into a simple 2D integral. It is valid in the same scales as the flat sky approximation which are the scales used in WL cosmology [26].

The assertion is that for a quantity in two dimensions defined as a weighted projection $x(\boldsymbol{\theta})$ from a 3D field $y(\chi\boldsymbol{\theta}, \chi)$ we have

$$x(\boldsymbol{\theta}) = \int_0^{\chi_s} d\chi\, W(\chi)\, y(\chi\boldsymbol{\theta}, \chi) \quad \Rightarrow \quad C_x(l) = \int_0^{\chi_s} d\chi\, \frac{W^2(\chi)}{\chi^2}\, \mathcal{P}_y\left(\frac{l}{\chi}\right). \tag{3.37}$$

For the specific case of Eq. 3.33, we will have the angular power spectrum [24]

$$C_\ell^{\kappa\kappa} = \int_0^{\chi_s} d\chi\, \frac{W^2(\chi)}{\chi^2}\, \mathcal{P}_\delta\left(k = \frac{\ell}{\chi}, \chi\right). \tag{3.38}$$

This directly relates convergence to the matter power spectrum, and consequently to cosmological parameters such as σ_8 and S_8. Convergence can be measured but it is harder, a more accessible measurement is the shear taken from the average ellipticity of galaxies. Fortunately, since shear and convergence arise from the same underlying field, we can show they have the same power spectrum.

To do that we take the deflection potential (Eq. 3.14) to the 2D Fourier space

$$\psi(\boldsymbol{\theta}) = \int \frac{d^2\ell}{(2\pi)^2}\,\psi(\boldsymbol{\ell})\,e^{i\boldsymbol{\ell}\cdot\boldsymbol{\theta}}, \tag{3.39}$$

From definitions of the WL parameters defined in Eq. 3.18

$$2\kappa(\boldsymbol{\ell}) = -\ell^2\psi(\boldsymbol{\ell}), \tag{3.40}$$

$$2\gamma_1(\boldsymbol{\ell}) = -(\ell_1^2 - \ell_2^2)\psi(\boldsymbol{\ell}) \tag{3.41}$$

$$\gamma_2(\boldsymbol{\ell}) = -\ell_1^2\ell_2^2\psi(\boldsymbol{\ell}) \tag{3.42}$$

We can see that in Fourier space convergence and shear relate as

$$4|\gamma(\boldsymbol{\ell})|^2 = [(\ell_1^2 - \ell_2^2)^2 + 4\ell_1^2\ell_2^2]|\psi(\boldsymbol{\ell})|^2 = (\ell_1^2 + \ell_2^2)^2|\psi(\boldsymbol{\ell})|^2 = 4|\kappa(\boldsymbol{\ell})|^2. \tag{3.43}$$

So finally [26]

$$C_\ell^{\gamma\gamma} = C_\ell^{\kappa\kappa}. \tag{3.44}$$

3.4 Observational Considerations

In practice surveys do not observe the convergence field $\kappa(\boldsymbol{\theta})$ directly. Instead, they measure approximate estimates of the reduced shear $g(\boldsymbol{\theta})$ from the shapes of distant galaxies. The fundamental observable is the complex ellipticity ϵ of each galaxy image, measured from pixel data after correcting for the instrumental point-spread function (PSF), detector effects and noise. In the weak regime and after averaging over many galaxies, the mean ellipticity provides an unbiased estimator of the reduced shear [26],

$$\langle\epsilon\rangle \simeq g \approx \gamma \quad \text{for} \quad |\kappa|, |\gamma| \ll 1. \tag{3.45}$$

Also, shape measurement algorithms introduce multiplicative and additive calibration biases that must be modeled and marginalised over [28].

Another detail that can add systematic error to the measurements is that they estimate redshifts using broad-band photometry. What enters the theory predictions is not the redshift of each individual galaxy, but the redshift distribution of sources in each tomographic bin [28],

$$n_i(z) \equiv \frac{dN_i}{dz}, \tag{3.46}$$

from which an effective lensing kernel $W_i(\chi)$ analogous to Eq. (3.34) is constructed. Calibrating $n_i(z)$ (using spectroscopic subsamples, clustering redshifts, or simulations) is one of the dominant systematics in weak lensing.

Also, in reality surveys often combine different signals [2]

- cosmic shear: shear–shear correlations between background galaxies (Sec.3.3)
- galaxy–galaxy lensing: shear of background sources around foreground lens galaxies, a direct probe of the halo-mass correlation ξ_{hm} (Sec.3.3)
- galaxy clustering: tracing ξ_{mm} through biased tracers.

The joint analysis of these three two point correlations is often called "3×2pt", and places tighter and more robust cosmological constraints than cosmic shear alone. Figure 3.3 shows a mass map reconstructed from 3×2pt data captured by the Dark Energy Survey.

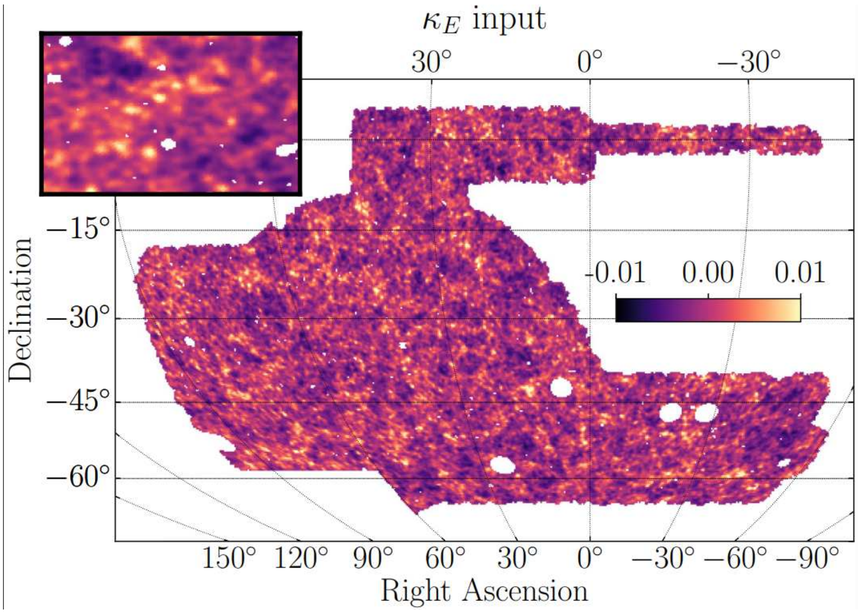

Figure 3.3: Mass map reconstructed from DES Year 3 shear observations. Source: Figure 3.3 in [29]

.

3.5 Weak Lensing in Cosmological Surveys

In recent years, the advent of large-area photometric and spectroscopic surveys—such as the Dark Energy Survey (DES), the Kilo-Degree Survey (KiDS), the Hyper Suprime-Cam (HSC), has revolutionized our ability to map the matter distribution across cosmic time. These surveys have provided unprecedented weak lensing data and galaxy cluster catalogs spanning vast cosmic volumes.

The first weak gravitational lensing applications targeted individual massive systems, such as galaxy clusters, where the shear signal is relatively large and can be mapped with modest data [30]. Shortly thereafter, the first detections of cosmic shear were reported using small-area ground-based surveys (of order a few square degrees) [31]. These early measurements demonstrated the feasibility of weak lensing as a cosmological probe, but suffered from:

- limited survey area (large sample variance),
- modest image quality (larger shape noise and PSF systematics),

- few photometric bands (poor redshift information).

The current generation of surveys, often called Stage III, has dramatically improved on these limitations. Key examples include: the Kilo-Degree Survey (KiDS) [1], Dark Energy Survey (DES) [2], Subaru Hyper Suprime-Cam survey (HSC) [3]. They cover hundreds to thousands of square degrees with high image quality and multi-band photometry, enabling tomographic weak lensing analyses with millions of source galaxies.

The main survey characteristics that drive the cosmological constraining power are:

- **Area** (in deg^2): controls sample variance and access to large angular scales.
- **Depth and limiting magnitude:** determine the source number density $n_{\rm eff}$ and median source redshift $z_{\rm med}$.
- **Image quality:** impacts the precision of shape measurements and PSF modeling.
- **Number and wavelength coverage of bands:** crucial for accurate photometric redshifts and $n_i(z)$.

These quantities set both the statistical uncertainties and the dominant systematics for each survey.

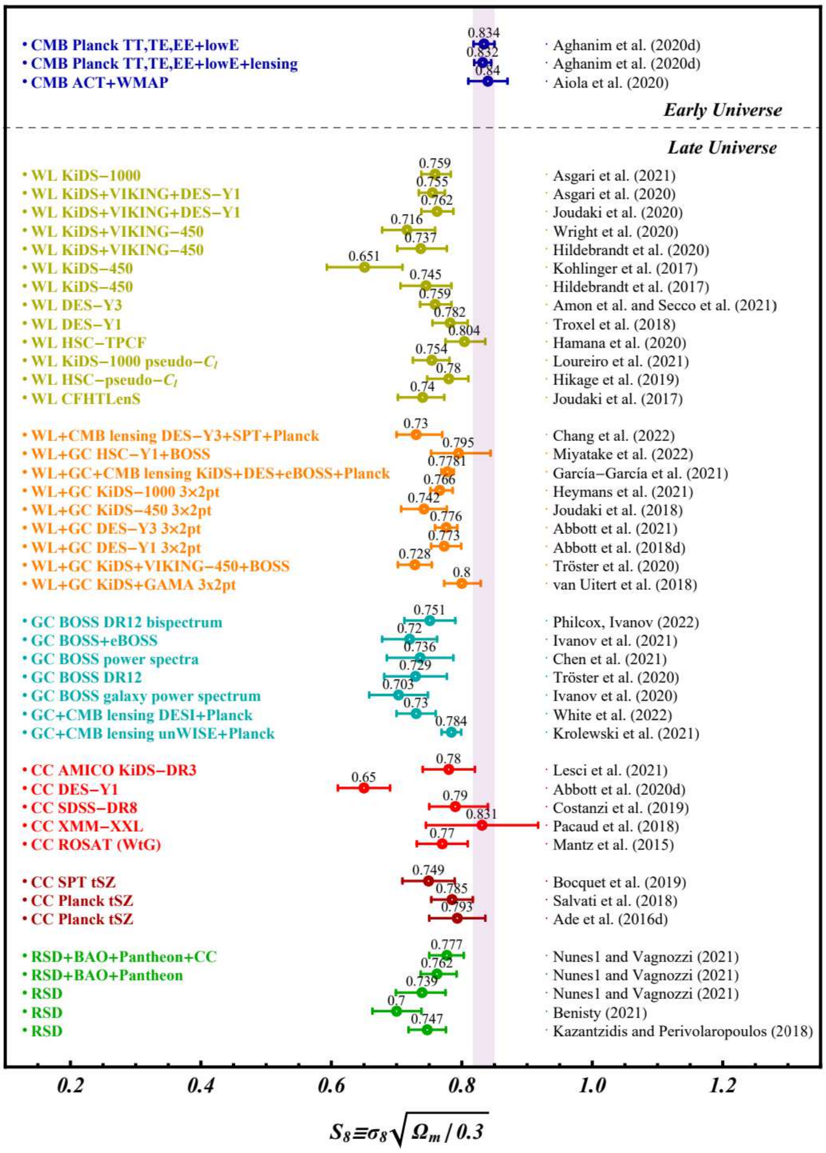

Figure 3.4: The value of S_8 from early and late universe measurements within 68% confidence level (WL = Weak Lensing, GC = Galaxy Clustering, CC = Cluster Counts, RSD = Redshift space distortion-Galaxy clustering). Source: Figure 3.4 in [9]

As discussed in Sec. 2.2, a convenient way to characterize the amplitude of matter clustering today is through the parameters σ_8 and S_8, which approximately follows the degeneracy direction to which weak lensing is most sensitive. A notable feature of recent cosmological analyses is that several weak lensing surveys have preferred values of S_8 somewhat lower than the value inferred from the CMB by the Planck satellite under ΛCDM. Planck 2018 finds $S_8 \simeq 0.83$ in the baseline model [7], while earlier Stage III weak lensing analyses typically reported $S_8 \simeq 0.75$ with uncertainties at the few-percent level, leading to a tension at the ~ 2–3σ level depending on the data sets and analysis choices [9]. Figure 3.4 show the values and error bars for early and late universe observations up to 2021.

This so-called S_8 tension could indicate: unaccounted systematics in one or more data sets (like shear calibration, photometric redshifts, intrinsic alignments, baryonic feedback), statistical fluctuations, or, more speculatively, new physics beyond ΛCDM affecting the late-time growth of structure. Clarifying the origin of this discrepancy is one of the main motivations for both improving modeling and obtaining better weak lensing data.

The KiDS survey recently added another observation to the puzzle. Earlier KiDS-1000 analyses, using ~ 1000 deg^2 of high-quality imaging and sophisticated photometric redshift calibration, found S_8 values around $S_8 \sim 0.76$, in ~ 3σ tension with Planck within ΛCDM. This strengthened the perception of a robust S_8 tension between early and late-time probes. More recently, the KiDS-Legacy analysis, which uses the completed KiDS data set and further improved modeling of systematics, has obtained a higher value of S_8 that is in good statistical agreement with Planck, with quoted tension at well below the 2σ level [32].

This updated result suggests that at least part of the earlier discrepancy may have been due to statistical fluctuations, analysis choices, or residual systematics, and illustrates how sensitive the inferred level of "tension" can be to methodological details. At the same time, other data sets and combined analyses still find somewhat low values of S_8, so there is not yet a unanimous picture.

The next major step in weak lensing cosmology will be the Legacy Survey of Space and Time (LSST) carried out by the Vera C. Rubin Observatory. LSST will image roughly $18\,000\,\mathrm{deg}^2$ of the southern sky in six optical bands over a period of ten years, reaching much fainter magnitudes and higher source densities than current Stage III surveys [4]. The Dark Energy Science Collaboration (DESC) is developing the analysis pipelines, simulations, and theoretical modeling required to exploit LSST data for cosmology [33].

From the perspective of weak lensing, LSST is expected to:

- deliver an order-of-magnitude increase in the number of source galaxies, enabling very precise measurements of $C_\ell^{\gamma\gamma}$ over a wide range of scales and redshifts;
- improve tomographic resolution, allowing a more detailed mapping of the growth of structure with redshift;
- enable powerful cross-correlations with galaxy clustering, CMB lensing and other probes, enhancing robustness to systematics;
- sharply reduce the statistical uncertainties on S_8 and other parameters, so that any residual discrepancy with Planck will be dominated by modeling and systematics rather than noise.

As a consequence, Rubin/LSST will play a decisive role in confirming whether the current hints of an S_8 tension are a sign of new physics or the result of hidden astrophysical and observational systematics.

Extracting cosmological information from these observations requires precise modeling of the matter distribution within halos. Uncertainties in the assumed density profiles can lead to biased inferences of cluster masses and, consequently, systematic shifts in cosmological parameters. This motivates a detailed reassessment of the commonly adopted profiles and the exploration of alternative models that may better capture the physical complexity of real halos as resolution increases with every generation of surveys.

4 DARK MATTER HALO DENSITY PROFILE

As seen in the previous Chapter, WL can be used as a tool to gain insight into Cosmology, and one of the ingredients necessary to model this phenomenon is the Density Profile ρ which represents the distribution of Dark Matter in a galaxy cluster. At the present time we lack an analytical solution for non-linear gravitational clustering and we turn ourselves to empirical laws derived and tested within the context of N-body simulations [20]. This results in a variety of different forms of ρ fitted to different contexts (mainly of scale, redshift and cosmology) with different assumptions. It is in this phenomenological landscape that this work resides.

The simplest approach to modeling halo density profiles begins by applying Newton's form of Kepler's Third Law to a test particle moving in a circular orbit within a spherically symmetric mass distribution. From the balance between gravitational and centripetal forces, the enclosed mass is

$$M(r) = \frac{v(r)^2 r}{G}, \tag{4.1}$$

where $v(r)$ is the velocity and r the distance from the center. Relating this to the density through the spherical mass integral,

$$4\pi \int_0^r \mathrm{d}r'\, r'^2 \rho(r') = \frac{v(r)^2 r}{G}, \tag{4.2}$$

and differentiating with respect to r, we obtain

$$\rho(r) = \frac{v(r)^2}{4\pi G r^2}\left(1 + 2\frac{d\log v(r)}{d\log r}\right) . \tag{4.3}$$

For a flat rotation curve ($v(r)$ =const), this reduces to a form closely resembling the Singular Isothermal Sphere (SIS) density profile. In the SIS model, the density is expressed in terms of the velocity dispersion σ_V, which quantifies the statistical spread of radial velocities:

$$\rho(r) = \frac{\sigma_V^2}{2\pi G r^2} .$$

The SIS profile is still a good fit for astrophysical phenomena in the scale of galaxies, and is what was used to accommodate Rubin's measurements of spiral galaxy rotation curves with Dark Matter [34, 35]. The rotation only makes sense with a spherical distribution of mass enclosing the galaxy, what we now denominate a Dark Matter Halo. However, with the advent of million particle N-body simulations in the early nineties, this simple profile did not comport the realizations specially for halos in the scale of galaxy clusters [36].

This was addressed by Navarro, Frenk and White in their 1996 seminal paper, and their model is still today the industry standard [36]. Since then, a series of other profiles were developed considering different ranges of mass and redshift in N-body simulations. More recently some models suggested the separation of the profile into an "inner" and an "outer" portion

$$\rho(r) = \rho_{\text{in}}(r) + \rho_{\text{out}}(r), \tag{4.4}$$

to account for the Halo's environment. Some of these approaches will be covered in this section.

4.1 Defying Halo Mass and Borders

Most modern uses of halo density profiles for cosmological purposes are obtained from N-Body simulations and, while not the theme of this work, it is useful to grasp the origins of the empirical laws that will be applied to observational and simulated data later [20].

N-body simulations evolve a dynamical system of particles in time under the influence of gravity. These particles evolve in a FLRW background with initial positions following a gaussian random field, as observed in the ΛCDM model for primordial fluctuations in the early Universe.

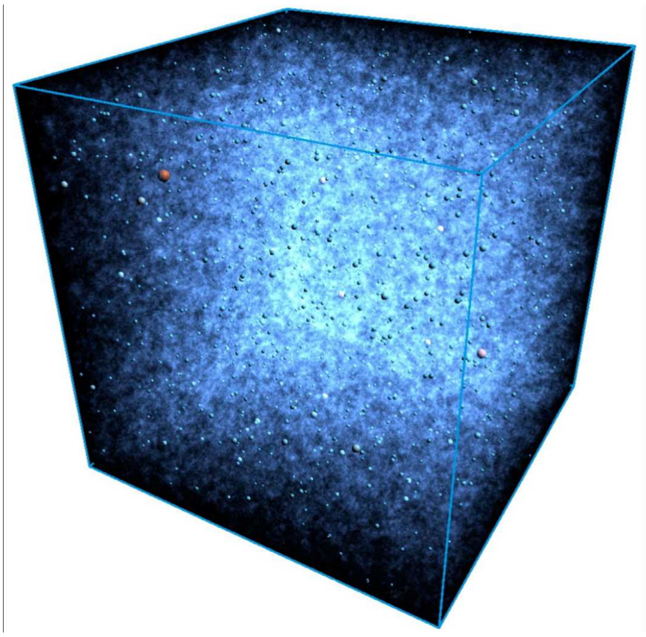

Figure 4.1: A vizualization of the Halos in the cosmoDC2 simulation at redshift $z = 0$. Source: Figure 1. in [37]

.

For illustration, the cosmoDC2 simulation (Figure 4.1), contains a trillion particles with masses of $1.85 \times 10^9\ h^{-1}M_{\odot}$ in a volume of $(3000\ h^{-1}\text{Mpc})^3$, simulating a patch of the sky similar in size to the visible sky in the south hemisphere [37].

The result of N-body simulations is a distribution of particles which can be translated as a mass density field. This has little connection with what is observed in surveys, since Dark Matter cannot be observed directly, and to make this connection we need to first identify the boundaries of individual halos in the simulation from which empirical laws describing density profiles can be found. Here we will present the two most used Halo Finder algorithms: Spherical Overdensity (SO) and Friend of

Friends (FoF) [20].

Spherical Overdensity

The SO algorithm usually identifies the center of the Halos as the minima in the gravitational potential. From that center, a sphere grows until a certain density threshold is met. This threshold is commonly set to be $\Delta = 180\bar{\rho}$, so it matches the virial overdensity predicted by the spherical collapse model, albeit $\Delta = 200\bar{\rho}$ is also a very commom choice.

Friend of Friends

The FoF algorithm does not assume any symmetry for the halo; particles are considered inside a halo if they are at a maximum distance from another particle that already composes the halo. This maximum distance is the only parameter and is called the "linking length". In cosmological applications, it is commonly set as $b = 0.2$ times the mean inter-particle separation given by $d = \sqrt[3]{N/V}$ for the N simulated particles in a co-moving volume V. Experience shows that halos with linking length $b = 0.2$ approximate an average enclosed density of $\Delta = 180\bar{\rho}$ as well.

A common procedure is to combine both techniques, applying FoF to identify particle groups and then define the center in which the SO algorithm will be applied. After defining the Halos in a simulation, we can propose general forms for the shape of the density profiles, that is, how dark matter is distributed inside dark matter halos, and compare this to the simulated result.

4.2 Inner Descriptions

Close to its center, a halo density profile can be described by what is called an "Inner Density Profile", approximating the distribution of dark matter close to the visible sources observed by traditional surveying methods. Here, we present some options we have to model this environment.

4.2.1 Navarro, Frenk and White's (NFW)

The problem faced by the NFW trio was the departure from the, at the time, high-resolution N-body simulations data from that which was expected with power law profiles such as SIS. They found that a smoothly changing logarithmic slope fitted their simulations better [36]:

$$\rho(r) = \frac{\rho_s}{\left(\frac{r}{r_s}\right)\left(1 + \frac{r}{r_s}\right)^2}. \tag{4.5}$$

Equation 4.5 introduces two parameters that should be fitted for each Halo, the scale radius r_s and the characteristic density ρ_s. Physically r_s indicates where the behavior of the profile changes, and becomes almost isothermal, as show in Figure 4.2. The profile is singular and the total mass diverges, but we can integrate to a certain radius, commonly set to be the virial radius, or the radius in which the density is $\Delta = 200\bar{\rho}$:

$$M = \int_0^r 4\pi\rho(r)\,dr = 4\pi\rho_s r_s^3\left[\ln\left(\frac{r_s + r}{r_s}\right) - \frac{r}{r_s + r}\right] \tag{4.6}$$

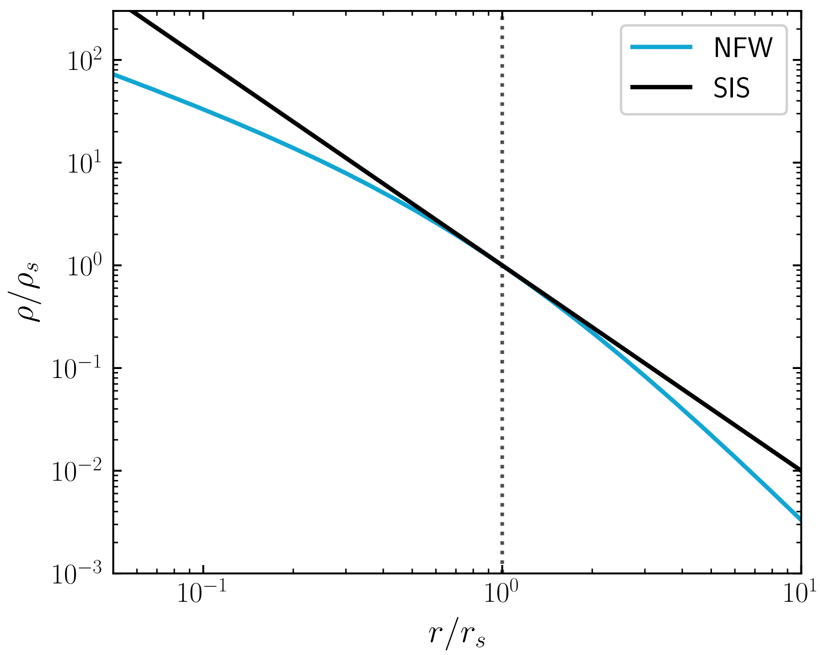

Figure 4.2: A comparison between an NFW and a SIS profile in the same conditions. Source: Profile implemented in Python by the author.

The logarithmic slope of the NFW model is -2 at $r = r_s$, but this can be generalized and has proven to be useful in certain contexts, such as galaxy cores and strong gravitational lensing [38]. The generalized NFW profile (gNFW) reads

$$\rho(r) = \frac{\rho_0}{\left(\frac{r}{r_s}\right)^{\gamma}\left[1 + \left(\frac{r}{r_s}\right)^{\alpha}\right]^{\frac{\beta-\gamma}{\alpha}}}, \tag{4.7}$$

where setting $\gamma = \alpha = 1$ and $\beta = 3$ results in the usual NFW profile. This is called the $\alpha\beta\gamma$, double power law, or gNFW profile, developed by [39] to encompass all the NFW-like profiles (Figure 4.3 shows some examples). Physically γ controls the slope near the center, β the slope at large radii, and α how quickly the transitions between these 2 regimes happen.

The program of the original NFW paper was to establish an Universal profile. Their main result was that their equation well matched Halos regardless of mass, solving the discrepancies of the old models in their newly accessible Halo resolutions. Their study explored a simulation with 10^6 particles, but still today the NFW profile shows good agreement with modern simulations, and its simplicity ensures its practicality when dealing with observational data.

4.2.2 Hernquist

The Hernquist model is a special case of $gNFW$, with $\gamma = \alpha = 1$ and $\beta = 2$ resulting in

$$\rho(r) = \frac{\rho_0}{\left(\frac{r}{r_s}\right)\left(1 + \frac{r}{r_s}\right)^3}.$$

Altough it is historically significant, modern uses in literature are hard to come across. It was proposed by Hernquist [40] in 1989 to describe the density profile of spherical galaxies, and was the profile used by NFW to fit their data initially, until they noticed that a slight modification of the Hernquist profile was beneficial. Figure 4.3 shows a comparison between a series of gNFW models including NFW and Hernquist.

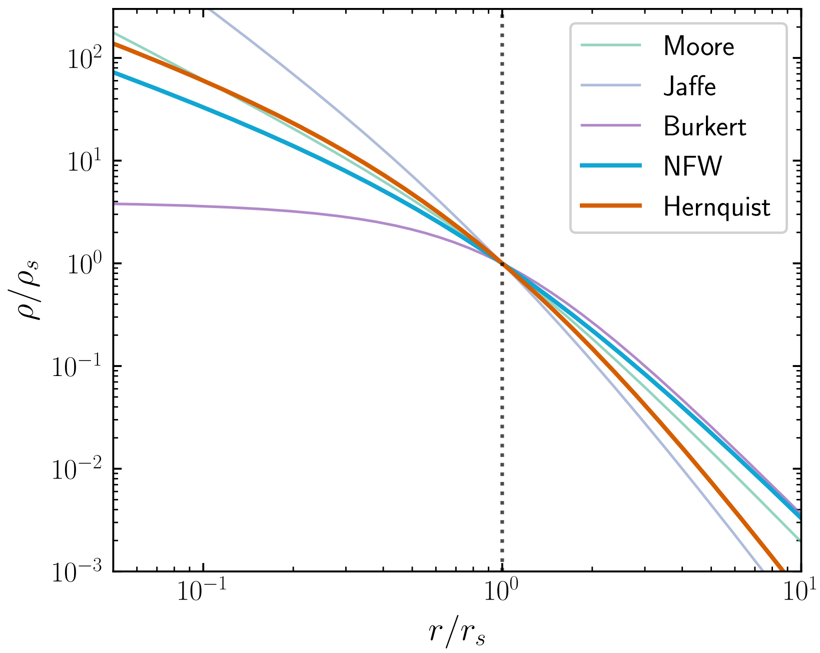

Figure 4.3: Profiles derived from gNFW 4.7, NFW and Hernquist highlighted. Moore $(\alpha, \beta, \gamma) = (1.5, 3, 1.5)$, Jaffe $(\alpha, \beta, \gamma) = (1, 4, 2)$, and Buckert $(\alpha, \beta, \gamma) = (1, 3, 0)$, are relevant in other astrophysical contexts but not commonly on cluster scales [38]. Source: Profiles implemented in Python by the author.

4.2.3 Einasto

The Einasto profile was developed in 1963 originally to describe the distribution of stars in the Milky Way. Now the logarithmic slope is not constant, but a function o the radius and a new parameter indicating how fast density decays from the center, established in the form [41]

$$\rho(r) = \rho_s \exp\left(-\frac{2}{\alpha}\left[\left(\frac{r}{r_s}\right)^{\alpha} - 1\right]\right).$$

The meaning of this profile is better understood with the derivative of its logarithm

$$\frac{d\log(\rho)}{d\log(r)} = -2\left(\frac{r}{r_s}\right)^{\alpha},$$

now we can control the derivative of the logarithmic curve, and have some freedom on the profile shape, but the cost of this is one more free parameter α.

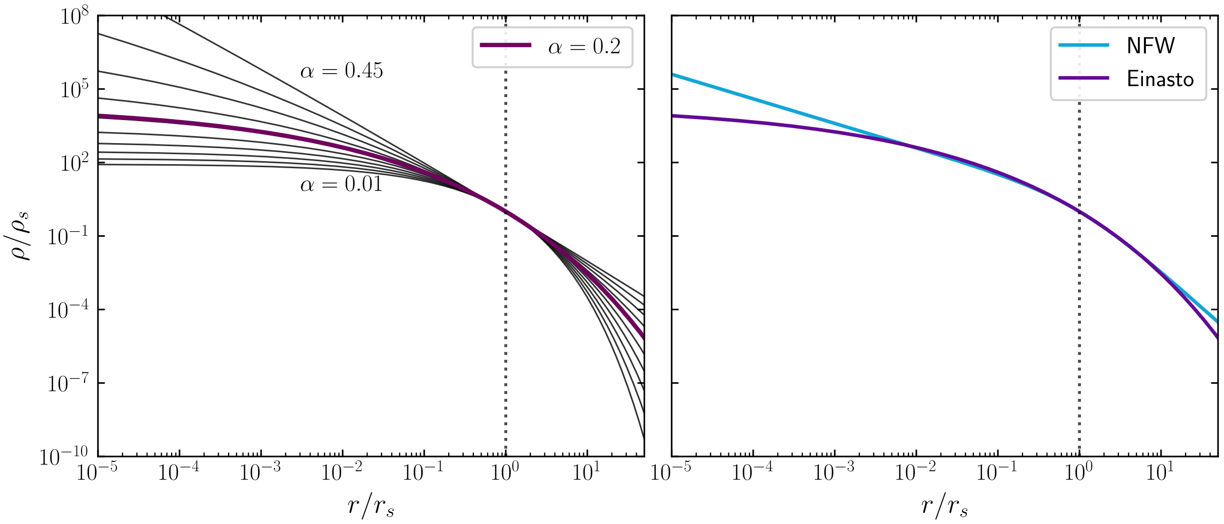

Figure 4.4: Left: Einasto profiles ranging from $\alpha = 0.01$ to $\alpha = 0.45$. Right: Comparison between an Einasto profile with $\alpha = 0.2$ and a NFW profile. Source: Profile implemented in Python by the author.

Although the solution for the total mass integral is more convoluted, it converges [22]. The total mass is given by

$$M = \frac{4\pi\rho_s r_s^3}{\alpha}\left(\frac{\alpha}{2}\right)^{3/\alpha}\Gamma(3/\alpha)\exp(2/\alpha), \tag{4.8}$$

where Γ denotes the Euler gamma function, $\Gamma(x) = \int_0^\infty t^{x-1}e^{-t}\,dt$.

The Einasto profile has been shown to equally or better adjust results in simulations [42]. Figure 4.4 shows a comparison of Einasto profiles with different α and an NFW profile. The parameter α can be fitted for each halo specifically such as ρ_s and r_s, but its physical meaning is not readily apparent.

Taking inspiration from the original NFW program, searching for a Universal density profile, Gao et al. [43] found an empirical law relating the parameter α to the spherical collapse model through the peak height ν. This empirical law relate these quantities with following equation

$$\alpha = 0.155 + 0.0095\nu^2. \tag{4.9}$$

Here α stops being a free parameter and is now only implicitly defined by redshift, halo mass, and the cosmological model since $\nu(M, z)$ as seen in section 2.4.

4.3 Outer Descriptions

Recently, the necessity for understanding how the Halo Density Profiles behave at large radii arose, because these regions are being probed in greater quantity and quality by Weak Lensing surveys with each generation of ground and space telescopes [33], and with the increase in resolution of N-body simulations, they are getting more realistic [44]. Here we present some of the options we have to model this environment, remembering that ρ_{out} is always a part of a sum with ρ_{in} to build the total density ρ.

4.3.1 Mean Density of the Universe

The first and most simple effect to be taken into account is that at large radii, the density of the Halo can be comparable to the mean density of the Universe. This can be corrected simply by taking the sum of our density profile with the mean density of the Universe, defined by

$$\rho_{\text{out}} = \rho_c. \tag{4.10}$$

Something to note is that adding this outer term to our profile makes it cosmology-dependent and causes the total mass to diverge.

4.3.2 2-Halo Term

One of the possibilities for modeling this exterior region is to take into account the interactions between neighboring Halos and how this affects their surroundings. This is accounted for by the procedure developed in section 2.6

$$\rho_{\text{out}} = \rho_m b(M)\xi_{hh}(r, z).$$

This effect becomes relevant at large radii $r \gtrsim 9r_{\text{vir}}$ [44], where the excess density due to neighboring Halos is more present, and the large-scale contribution begins to dominate.

4.3.3 Power Law

For relatively small radii $r \lesssim 9r_{\text{vir}}$, the 2-Halo outer term can be approximated by a simple power law [44]

$$\rho_{\text{out}}(r) = \rho_{\text{m}}(z)\frac{a}{\frac{1}{m} + \left(\frac{r}{r_p}\right)^b}. \tag{4.11}$$

Here three parameters are introduced for the outer profile: a is a normalization constant, b is the logarithmic slope, m is the maximum contribution this profile can make to the total mass sum, and r_p is the fixed radius where the effects begin to take place; without it, we would have spurious density contributions close to the Halo center.

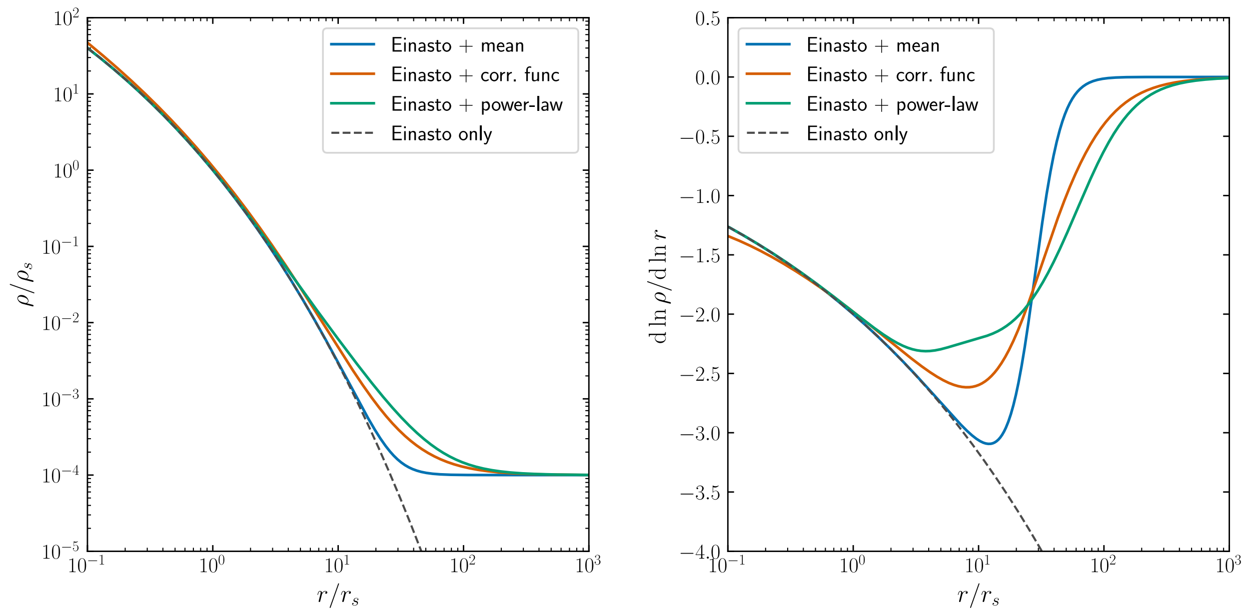

Figure 4.5: Comparisons between an Einasto profile coupled with different outer profiles. Left: log density plot. Right: logarithmic derivative. Source: Profile implemented in Python by the author.

4.4 Compound Descriptions

The division into an inner and outer part gives some modularity to our Halo Density Profile, we can choose one of the Inner descriptions and one or a combination of Outer descriptions. Besides those liberties, there are arguments to use a physically motivated profile in a full coherent view, encompassing the inner and outer descriptions.

4.4.1 Diemer and Kravtov Truncated Exponential (DK14)

Diemer and Kravtov noticed a significant departure from universal profiles such as NFW in their simulations, particularly, for massive or rapidly accreting halos at radii $r \gtrsim 0.5\, r_{200m}$. What they found was a more sharp steepening decay than they predicted, that increased proportionately with peak height ν [44].

They trace this behavior to the mass accretion rate of these profiles, defined as

$$\Gamma \equiv \frac{\Delta \log(M_{\rm vir})}{\Delta \log(a)}. \tag{4.12}$$

This quantifies how fast the halo mass increases with time. DK14 [44] shows that it serves as a proxy for halo accretion and merger histories in the simulation. In conclusion, they successfully map peak height ν to Γ (more massive halos accrete matter more rapidly), and to the steepening of the logarithmic derivative of these profiles.

The accretion rate is a measurement only possible within the N-body simulation, so DK14 propose a fitting function to model the phenomenon. They utilize the Einasto Profile as their Inner

Description, and for the Outer profile, a combination of the mean density of the Universe with a power law or 2-halo term, depending on the range explored, but with a difference, it is added a term f_{trans} to describe the transition between both regimes. As such

$$\rho(r) = \rho_{\text{in}}\, f_t + \rho_{\text{out}}$$

$$f_{\text{trans}} = \left[1 + \left(\frac{r}{r_{\text{t}}}\right)^{\beta}\right]^{-\frac{\gamma}{\beta}},$$

What f_{trans} achieves is the steepening of the profile around a truncation radius r_t, where γ is the logarithmic derivative at radius $r = 200$ and β defines how quickly it reaches it.

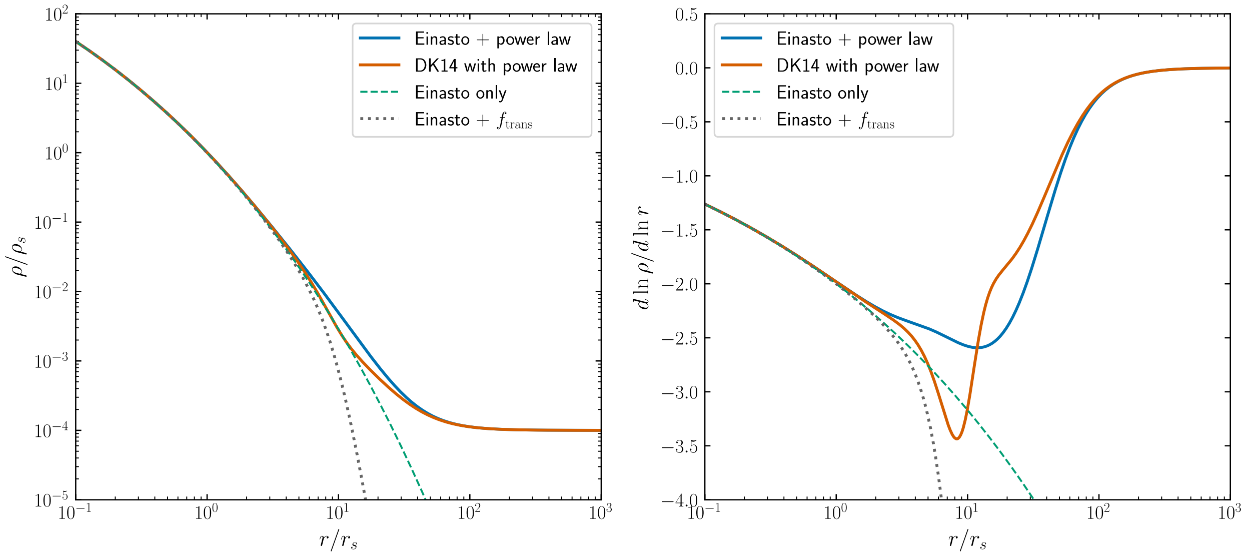

Figure 4.6: Comparisons between an Einasto and power law profile with DK14. Left: log density plot. Right: logarithmic derivative. Source: Profile implemented in Python by the author.

The results of DK14 is interesting; halos are still virialized and spherically symmetrical in this context, but their evolution left a mark on their density profile. The physical origin of this phenomenon was not clearly understood until an advancement came with Diemer's 2022 halo density profile [45].

Diemer [45] evolved the DK14 profile, instead of using the mass accretion rate to proxy the merger and accretion history he follows the dynamical paths accreted particles in the simulation, and notices that they accumulate in orbits around the truncation radius given by DK14. From that he proposes a new fit for the profile:

$$\rho(r) = \rho_s \exp\left\{-\frac{2}{\alpha}\left[\left(\frac{r}{r_s}\right)^{\alpha} - 1\right] - \frac{1}{\beta}\left[\left(\frac{r}{r_t}\right)^{\beta} - \left(\frac{r_s}{r_t}\right)^{\beta}\right]\right\}, \tag{4.13}$$

this profile has 5 free parameters and does not receive an outer profile. In first analysis it does not improve accuracy, but it gives better physical meaning for the phenomenon observed.

4.5 Mass Definitions

Although it is possible to fit each halo to a pair of scaled density and scale radius, this is not common practice. Profiles are more naturally described by a mass definition and a concentration

$$c_\Delta \equiv \frac{r_\Delta}{r_s}. \tag{4.14}$$

The mass is defined by a spherical overdensity such that

$$M_\Delta = \frac{4\pi}{3}\Delta\rho_{\text{ref}} R_\Delta^3. \tag{4.15}$$

So we fix a mass and radius to contain a density. There are several definitions of $\Delta\rho_{\text{ref}}$, inspired by the spherical collapse it can be in terms of the mean density of the Universe $200 \times \rho_m$ or $178 \times \rho_m$, or in terms of the virial density we get from the virial radius. It is also common to define it in terms of the critical density of the universe $\Delta\rho_c$, here values of 200, 500 up to 2500 for Δ are common [22].

For our profiles, the scale radius is them, depending on the mass definition of choice and the concentration,

$$r_s \equiv \frac{r_\Delta}{c_\Delta}. \tag{4.16}$$

Another approach to this is to try to find a direct relation between concentration and mass, the $c - M$ relation. It turns out these models depend non-trivially on redshift and cosmology, and present high halo-to-halo scatter. A comprehensive study of several models of $c - M$ as well as their impact on weak lensing measurements is given in a related thesis to this one [46].

5 IMPLEMENTATION RESULTS

The previous chapters defined different models for the halo density profile, discussed their role within the broader context of cosmology, and described how they relate to cosmological observables. Now we turn ourselves to the practical implementation in code libraries used for the analysis of observational and simulated data.

5.1 COMPUTATIONAL TOOLS

We compare the results from two code libraries: NumCosmo (Numerical Cosmology Library) [47], and Colossus (Cosmology, Halo, and Large Scale Structure Tools) [48], logos for both libraries are shown in Fig. 5.1. Not all profiles are implemented in NumCosmo, therefore, some results presented here combine native NumCosmo outputs with externally implemented extensions, but it will be clear in the text when this happens. This is the first step for implementing all the profiles natively in NumCosmo, because this enables the use of NumCosmo's end-to-end cosmological pipeline with the newly implemented profiles.

Figure 5.1: Left: the logo for the Numcosmo library [49]. Right: the logo for the Colossus library [50].

5.1.1 NumCosmo

NumCosmo is a general-purpose cosmology library, written in C, that provides statistical tools to test cosmological models. The following is the official description from the documentation [47]:

> NumCosmo is a free software C library whose main purposes are to test cosmological models using observational data and to provide a set of tools to perform cosmological calculations. The software implements three different probes: cosmic microwave background (CMB), supernovae type Ia (SNeIa) and large-scale structure (LSS) information, such as baryonic acoustic oscillations (BAO) and galaxy cluster abundance. The code supports a joint analysis of these data and the parameter space can include cosmological and phenomenological parameters. NumCosmo

> matter power spectrum and CMB codes were written independent of other implementations such as CMBFAST, CAMB, etc.
>
> The library structure simplifies the inclusion of non-standard cosmological models. Besides the functions related to cosmological quantities, this library also implements mathematical and statistical tools. The former were developed to enable the inclusion of other probes and/or theoretical models and to optimize the codes. The statistical framework comprises algorithms which define likelihood functions, minimization, Monte Carlo, Fisher Matrix and profile likelihood methods.

A recent addition to the code base is the description of halo density profiles, and the derived calculations of surface mass density and shear to model weak lensing by galaxy clusters. It is very important for cosmological surveys to utilize more than one independent pipeline for data analysis to mitigate the possibility of systematic errors. For this reason, the NumCosmo library is one of the backend options of the Cluster Lensing Mass Modeling library (CLMM) [51].

The CLMM library is a Python toolkit developed by members of the LSST-DESC collaboration for performing galaxy cluster mass reconstruction from weak lensing observables, crucial to mass calibration. It was built in anticipation of the data releases of the coming survey carried out by the Vera C. Rubin Observatory.

5.1.2 Colossus

Colossus is a Python toolkit for cosmology, specialized in the large-scale structure and the properties of dark matter halos. Although it is more limited in scope, it contains the latest developments in halo density profiles. The official module structure is summarized below.

> Colossus consists of three top-level modules:
>
> - Cosmology: Implements ΛCDM cosmologies with curvature, relativistic species, and different dark energy equations of state. Includes standard calculations such as densities and times, but also more advanced computations such as the power spectrum, variance, and correlation function.
> - Large-scale structure: Deals with peaks in Gaussian random fields and the statistical properties of halos such as peak height, peak curvature, halo bias, and the mass function.
> - Dark matter halos: Deals with halo masses and radii in arbitrary spherical overdensity definitions, pseudo-evolution, implements general and specific halo density profiles (Einasto, Hernquist, NFW, DK14, etc), computes models for halo concentration and the splashback radius.

5.2 Cosmology and Halo Definitions

In both libraries, the background cosmology is set to the Planck 2018 best-fit parameters [7] (their Table 2 column 6). Halo properties are specified using spherical-overdensity mass definitions. For each case, halo profiles are compared at fixed halo mass and redshift.

Specifically, we consider the combinations representing low, usual, and high values for z and M commonly explored in galaxy cluster surveys

$$z \in \{0.6,\ 0.9,\ 1.2\}, \qquad M_{\mathrm{vir}} \in \{5 \times 10^{13},\ 10^{14},\ 5 \times 10^{14},\ 10^{15}\}\ M_{\odot}, \tag{5.1}$$

resulting in a total of twelve independent halo realizations.

The numerical comparison between NumCosmo and Colossus is quantified using the absolute relative difference

$$\left| \frac{\rho_{\mathrm{nc}}(r)}{\rho_{\mathrm{col}}(r)} - 1 \right|, \tag{5.2}$$

where ρ_{nc} is the density computed with NumCosmo (including external extensions when necessary) and ρ_{col} is the density computed with Colossus.

An important metric will be the maximum absolute relative difference

$$\max \left| \frac{\rho_{\mathrm{nc}}(r)}{\rho_{\mathrm{col}}(r)} - 1 \right|, \tag{5.3}$$

and also the root mean square (RMS) of the absolute relative difference, defined as

$$\mathrm{RMS} \equiv \sqrt{\frac{1}{N} \sum_{i=1}^{N} \left[\left| \frac{\rho_{\mathrm{nc}}(r_i)}{\rho_{\mathrm{col}}(r_i)} - 1 \right| \right]^2}, \tag{5.4}$$

where the sum runs over the N sampled radial points r_i. While the maximum relative difference highlights the worst local disagreement between the two implementations, the RMS provides a global measure of the typical discrepancy across the full radial range.

The two libraries use different native units for density:

$$[\rho_{\mathrm{col}}] = \frac{M_{\odot} h^2}{\mathrm{kpc}^3}, \qquad [\rho_{\mathrm{nc}}] = \frac{M_{\odot}}{\mathrm{Mpc}^3}. \tag{5.5}$$

All Colossus outputs are converted to NumCosmo units using the factor

$$h^2 \times 10^9. \tag{5.6}$$

5.3 Library Comparisons

This section presents the relative difference charts of the implementations together with the maximum difference and the RMS. A more detailed discussion will come at the end of every profile in a summary section.

All the code written is available at a public GitHub repository in this link, containing the code for the both libraries, as well as the external extension, and the visualizations created on the last chapter.

5.3.1 Inner Profiles

All inner profiles are already natively implemented in NumCosmo, so for this subsection, the comparison is direct between the two libraries.

NFW

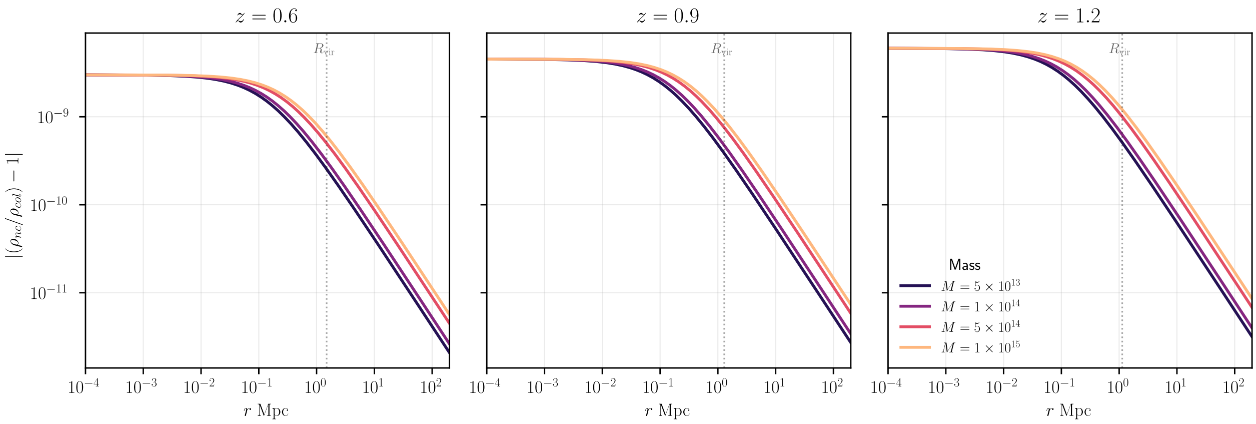

Figure 5.2: Relative differences between the NFW profiles generated by Numcosmo and by Colossus across redshifts and masses in Eq. 5.1.

Across all masses and redshifts the NFW implementations have good agreement. Fig. 5.2 shows that the difference is nearly flat at small radii around 10^{-9}, decreasing smoothly beyond the scale radius.

Quantitatively, the maximum relative difference observed is

$$\max \left| \frac{\rho_{\rm nc}(r)}{\rho_{\rm col}(r)} - 1 \right| = 6.003 \times 10^{-9} \qquad (z = 1.2), \tag{5.7}$$

while the RMS relative difference over the full radial range is

$$\text{RMS} = 3.137 \times 10^{-9}, \tag{5.8}$$

Hernquist

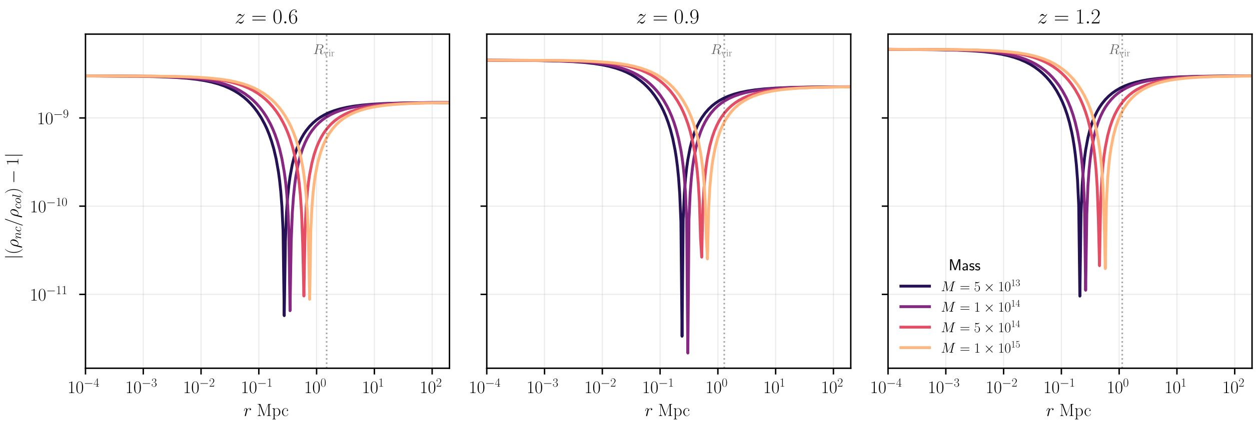

Figure 5.3: Relative differences between the Hernquist profiles generated by Numcosmo and by Colossus across redshifts and masses in Eq. 5.1.

The Hernquist implementations show similar precision as NFW. Fig. 5.3 shows a steady difference around 10^{-9} for the range of mass and redshift studied, but with an artifact of the relative difference crossing zero, indicating a sign change.

Quantitatively, the maximum relative difference observed is

$$\max\left|\frac{\rho_{\rm nc}(r)}{\rho_{\rm col}(r)} - 1\right| = 6.002 \times 10^{-9} \qquad (z = 1.2), \tag{5.9}$$

while the RMS relative difference over the full radial range is

$$\text{RMS} = 3.254 \times 10^{-9}, \tag{5.10}$$

Einasto

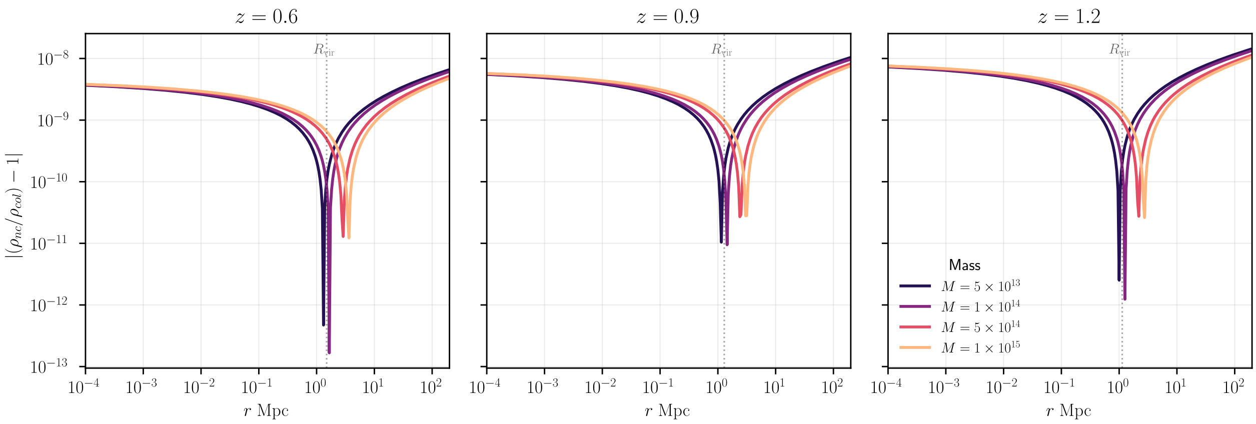

Figure 5.4: Relative differences between the Einasto profiles generated by Numcosmo and by Colossus across redshifts and masses in Eq. 5.1.

Einasto has a free parameter that was set to $\alpha = 0.18$ in both libraries, although a future analysis using the form given in Eq. 4.9 is due. The implementations show agreements around 10^{-8} beyond the virial radius, and similar behavior as Hernquist, with Fig. 5.4 also showing the agreements crossing signs.

Quantitatively, the maximum relative difference observed is

$$\max\left|\frac{\rho_{\rm nc}(r)}{\rho_{\rm col}(r)} - 1\right| = 1.437 \times 10^{-8} \qquad (z = 1.2), \tag{5.11}$$

while the RMS relative difference over the full radial range is

$$\text{RMS} = 4.386 \times 10^{-9}, \tag{5.12}$$

5.3.2 Outer Profiles

Outer profiles are not implemented in NumCosmo, so for mean density, power law, and 2-halo, We wrote their function in Python to couple with NumCosmo results. An important point when coupling these outer profiles to the inner profiles NumCosmo has, is that when we create them using mass definitions, the profile will not be a simple addition of the form

$$\rho = \rho_{in} + \rho_{out}. \tag{5.13}$$

In this case, we need to add the outer profile and rescale everything to match the given mass and concentration. Colossus does this natively, while for NumCosmo we implemented this externally as

$$\rho_{\rm tot}(r) = \underbrace{\left(\frac{M_\Delta - M_{\rm out}(r_\Delta)}{M_{\rm in}(r_\Delta)}\right)}_{\text{mass–preserving scale factor}} \rho_{\rm in}(r) \; + \; \rho_{\rm out}(r), \tag{5.14}$$

with

$$M_{\rm in}(r_\Delta) = \int_0^{r_\Delta} 4\pi r^2\, \rho_{\rm in}(r)\, dr, \qquad M_{\rm out}(R_\Delta) = \int_0^{R_\Delta} 4\pi r^2\, \rho_{\rm out}(r)\, dr, \tag{5.15}$$

in this specific case $M_\Delta = M_{in}$, we applied this rescaling for all profiles generated with NumCosmo + externally implemented outer profile. The integration is carried out with the scientific computing Python library NumPy using the composite trapezoidal rule.

Mean Density

The mean density has a redshift dependency, in Table 5.1 the output values given by each library are compared.

Table 5.1: Comparison of the mean matter density $\rho_m(z)$ computed with NumCosmo and Colossus, for the redshifts considered in this work. Both results are expressed in units of $M_\odot\,\mathrm{Mpc}^{-3}$. The absolute and relative differences demonstrate numerical agreement at the level of floating-point precision.

z	$\rho_m^{\mathrm{NC}}(z)$	$\rho_m^{\mathrm{Col}}(z)$	$\lvert\Delta\rho_m\rvert$	$\lvert\Delta\rho_m\rvert/\rho_m^{\mathrm{Col}}$
0.60	1.618990×10^{11}	1.618990×10^{11}	7.156×10^{-2}	4.420×10^{-13}
0.90	2.711097×10^{11}	2.711097×10^{11}	1.199×10^{-1}	4.422×10^{-13}
1.20	4.208742×10^{11}	4.208742×10^{11}	1.862×10^{-1}	4.423×10^{-13}

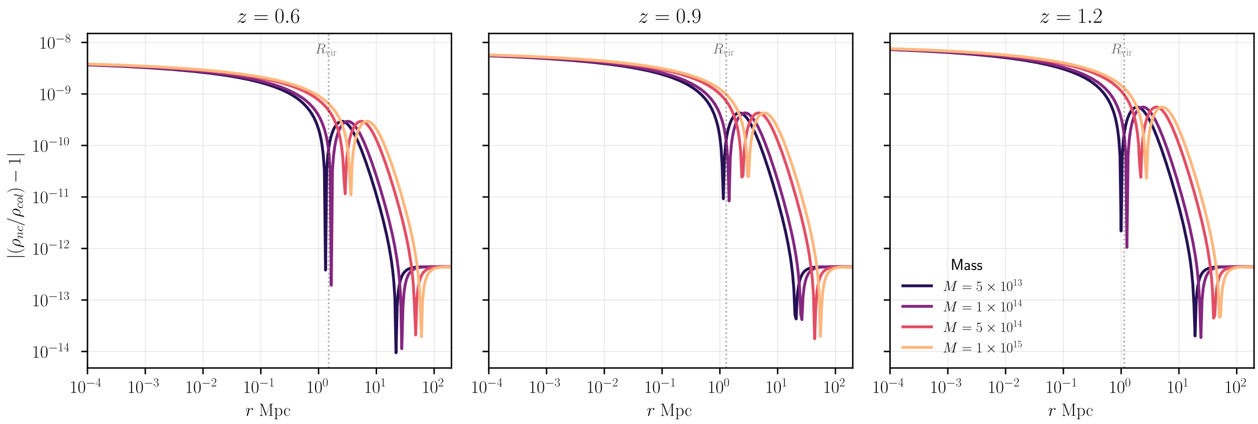

Figure 5.5: Relative differences between the Einasto coupled with mean density profiles generated by NumCosmo (with an externally implemented portion) and by Colossus across redshifts and masses in Eq. 5.1.

Figure 5.5 indicates that the addition of the outer profile does not cause any systematic error, with the relative difference remaining around 10^{-9}. The "dip" features of Einasto remain, and another crossing appears around the radius where the outer term dominates.

Quantitatively the maximum relative difference observed is

$$\max\left|\frac{\rho_{\mathrm{nc}}(r)}{\rho_{\mathrm{col}}(r)} - 1\right| = 7.574 \times 10^{-9} \qquad (z = 1.2), \tag{5.16}$$

while the RMS relative difference over the full radial range is

$$\mathrm{RMS} = 3.339 \times 10^{-9}, \tag{5.17}$$

Power Law

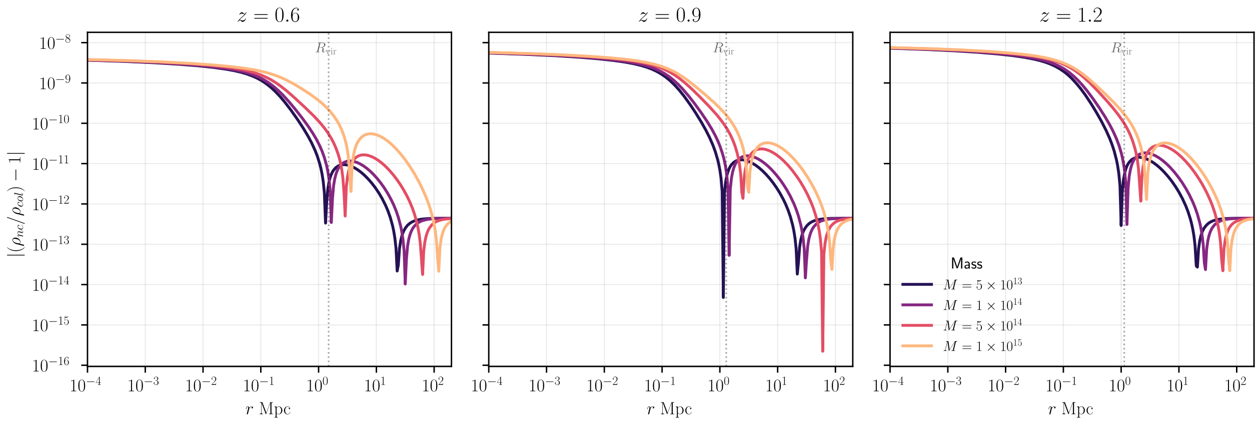

Figure 5.6: Relative differences between the Einasto coupled with power law density profiles generated by Numcosmo (with an externally implemented portion) and by Colossus across redshifts and masses in Eq. 5.1.

The power law outer profile free parameters were set to

$$a = 1, \qquad b = 2, \qquad r_t = 14.7, \qquad m = 1000\,. \tag{5.18}$$

The relative difference between the Einasto coupled with a power law outer profile are dominated by the outer term, as shown in Fig. 5.6, with higher differences around 10^{-6}. The residuals are smooth and monotonic with radius, with the largest discrepancies occurring at small radii and progressively decreasing toward large radii. This behavior is consistent across all halo masses and redshifts, indicating a systematic but controlled difference between the two implementations.

Quantitatively the maximum relative difference observed is

$$\max\left|\frac{\rho_{\rm nc}(r)}{\rho_{\rm col}(r)} - 1\right| = 7.569 \times 10^{-9} \qquad (z = 1.2), \tag{5.19}$$

while the RMS relative difference over the full radial range is

$$\text{RMS} = 3.223 \times 10^{-9}, \tag{5.20}$$

Correlation Function

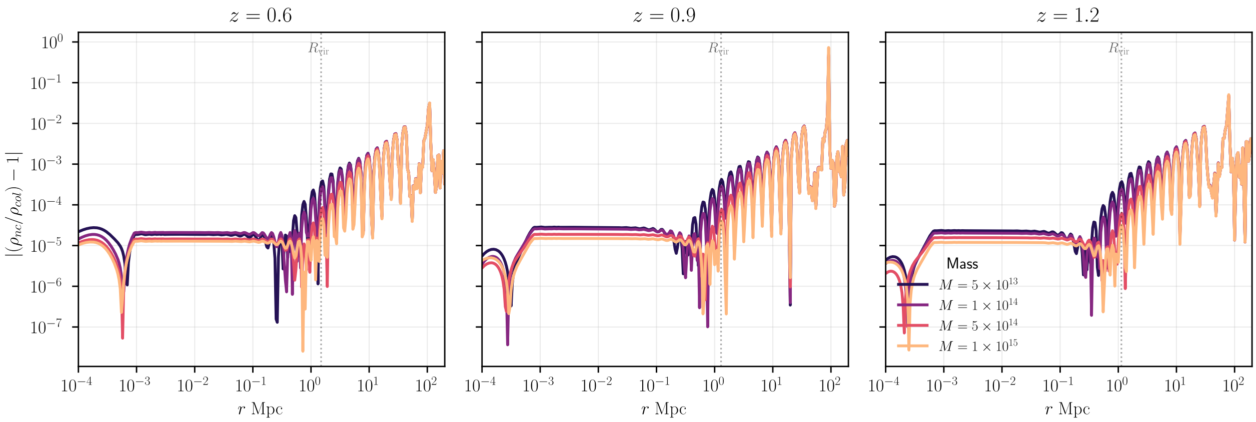

Figure 5.7: Relative differences between the Einasto coupled with 2-halo term density profiles generated by NumCosmo (with an externally implemented portion) and by Colossus across redshifts and masses in Eq. 5.1.

We calculated the two-halo contribution using the native correlation functions of each library with a fixed bias value of $b = 5$. The results in Fig. 5.7 show that the agreement is no longer uniformly excellent over the full radial range. For all redshifts and masses, the relative difference remains approximately at the 10^{-5} level from intermediate radii up to about $r \sim 10^0\,\mathrm{Mpc}$, indicating that the profiles are still broadly consistent in this regime. However, beyond this scale, especially around and above R_{vir}, the curves develop increasingly large oscillatory features and eventually reach clearly incorrect values, showing that the large-radius behavior is not yet under control.

The most problematic case occurs at $z = 0.9$, where the maximum relative difference reaches

$$\max\left|\frac{\rho_{\mathrm{nc}}(r)}{\rho_{\mathrm{col}}(r)} - 1\right| = 7.308 \times 10^{-1}, \qquad (z = 0.9), \tag{5.21}$$

while the corresponding RMS relative difference is

$$\mathrm{RMS} = 1.760 \times 10^{-2}. \tag{5.22}$$

Therefore, although the two implementations remain consistent at the $\sim 10^{-5}$ level over part of the radial domain, the disagreement at larger radii shows that the present 2-halo comparison is still incomplete. This behavior suggests that further investigation is required to identify the origin of the mismatch and to make the large-scale implementation fully reliable.

DK14

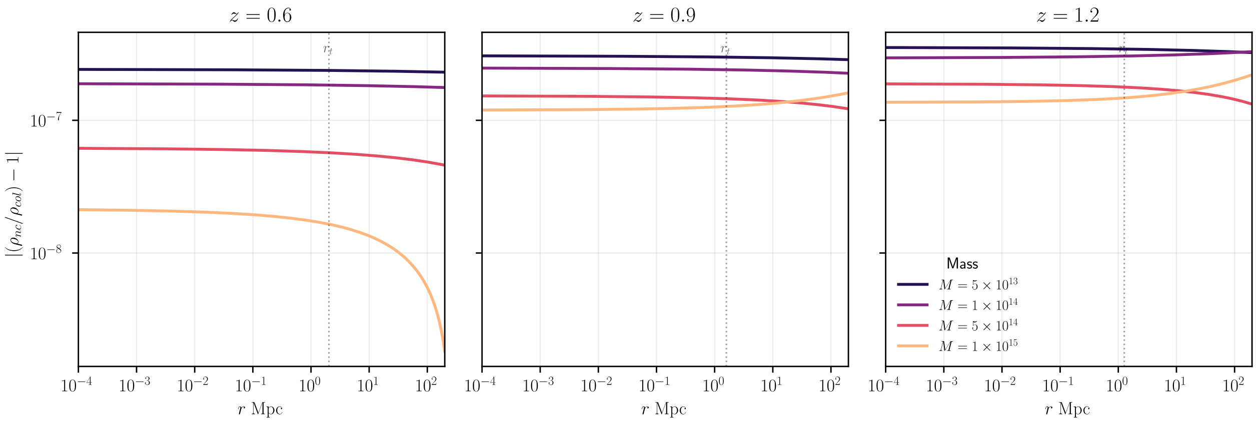

Figure 5.8: Relative differences between the inner part of the DK14 density profiles generated by Numcosmo (with an externally implemented portion) and by Colossus across redshifts and masses in Eq. 5.1.

Figure 5.8 shows the relative differences between the inner part of the DK14 profile $\rho_{in} f_t$ for visualization, but it should be noted that the DK14 profile should always be coupled with one the outer profiles defined previously. Now the mass preserving factor is not applied on the outer profile, but on the transfer function itself.

The Colossus library has means of estimating the parameters of the transfer function based on the mass and accretion rate bins defined in the original paper [44]. At present, these values are extracted from Colossus and replicated to the custom implementation of the transfer function. They are

$$\alpha = 0.25, \qquad \beta = 4, \qquad \gamma = 8, \tag{5.23}$$

so we used the base NumCosmo Einasto profile with $\alpha = 0.25$, and a transfer function with the other parameters.

DK14 shows almost steady relative differences, remaining at 10^{-7}-10^{-6}, this shows that the transfer function differences are an order of magnitude above the ones shown the Einasto only profiles at 10^{-8}, being comparable with the Einasto + Power Law profiles.

Quantitatively the maximum relative difference observed is

$$\max\left|\frac{\rho_{\rm nc}(r)}{\rho_{\rm col}(r)} - 1\right| = 3.537 \times 10^{-7} \qquad (z = 1.2), \tag{5.24}$$

while the RMS relative difference over the full radial range is

$$\text{RMS} = 2.137 \times 10^{-7}. \tag{5.25}$$

5.3.3 Summary

Taken together, the results presented in this chapter demonstrate a high level of numerical consistency between the halo density profiles implemented in NumCosmo and those provided by Colossus, across all redshifts and halo masses considered in Eq. (5.1). For profiles that are natively implemented in both libraries, namely the NFW, Hernquist, and Einasto inner profiles, the agreement is excellent, with maximum absolute relative differences at the level of 10^{-9} to 10^{-8} (Tab. 5.2). These discrepancies are consistent with machine-level numerical effects arising from floating-point arithmetic, numerical integration, and minor implementation differences, rather than from any physical mismatch.

Table 5.2: Summary of the maximum and root mean square (RMS) absolute relative differences between halo density profiles computed with NumCosmo and Colossus, considering all radial points, halo masses, and redshifts analyzed in this work.

Profile	max	RMS
NFW	6.003×10^{-9}	3.137×10^{-9}
Einasto	1.437×10^{-8}	4.386×10^{-9}
Hernquist	6.002×10^{-9}	3.254×10^{-9}
Einasto + mean	7.574×10^{-9}	3.339×10^{-9}
Einasto + power law	7.569×10^{-9}	3.223×10^{-9}
Einasto + 2-halo	7.308×10^{-1}	1.760×10^{-2}
DK14	3.537×10^{-7}	2.137×10^{-7}

When outer components are introduced, the behavior depends on the structural complexity of the model. The Einasto profile coupled to a constant mean density outer term shows discrepancies comparable to the pure inner profiles, indicating that the mass-preserving rescaling implemented externally for NumCosmo faithfully reproduces the normalization procedure adopted in Colossus.

The Einasto profile combined with a power-law outer term also shows excellent agreement, with maximum and RMS relative differences remaining at the 10^{-9} level. This indicates that the externally implemented power-law contribution is numerically stable and consistent with the Colossus reference over the full range of radii, halo masses, and redshifts considered here.

The DK14 profile exhibits larger discrepancies than the previous cases, but still remains in very good agreement overall, with maximum and RMS relative differences at the 10^{-7} level. In practice, this means that even for a more structurally complex profile, involving truncation and additional radial dependence, the NumCosmo implementation remains highly consistent with Colossus.

The main exception is the Einasto + 2-halo case. Although the comparison remains well behaved over part of the radial range, with relative differences staying around the 10^{-5} level up to approximately $r \sim 10^0\,\mathrm{Mpc}$, the large-radius behavior becomes unreliable. In particular, beyond this scale the curves develop increasingly large oscillatory features and eventually reach clearly incorrect values, leading to a maximum relative difference of 7.308×10^{-1} and an RMS of 1.760×10^{-2}. Therefore, unlike the other models, the 2-halo implementation still requires further investigation before it can be considered fully validated. This suggests that some aspect of the large-scale treatment, such as the correlation-function evaluation, normalization, radial convention, or matching between the inner Einasto term and the 2-halo contribution, is still not fully under control.

Overall, no systematic trends with redshift or halo mass are observed in the well-behaved comparisons. Excluding the current issues in the 2-halo case, the results indicate that the NumCosmo implementations, including the externally implemented outer profiles, are robust across the full range of halo properties explored in this work. The hierarchy of numerical discrepancies across models is broadly correlated with the structural complexity of the profile construction, while the anomalous behavior of the 2-halo term points to a specific implementation issue rather than a general inconsistency between the two libraries.

6 CONCLUSION AND FURTHER DEVELOPMENTS

Precision cosmology has advanced dramatically since the early 2000s. Over the last two decades, increasingly accurate observations and large scale numerical simulations, significantly improved the quantitative testing of cosmological models. In this context, the consistency of theoretical modeling across independent computational tools has become a critical requirement. Uniform definitions, transparent conventions, and cross-validation between publicly available libraries are essential to ensure one of the foundational principles of science: reproducibility.

In this work, we reviewed several halo density profiles proposed in the literature and performed a detailed numerical comparison of their implementations in two widely used cosmological libraries, NumCosmo and Colossus. By comparing independent implementations at fixed halo mass and redshift, we quantified the level of numerical agreement across a representative range of halo properties relevant for current and upcoming surveys. The results demonstrate that for inner halo profiles natively implemented in both libraries, such as NFW, Hernquist, and Einasto, the agreement reaches the level expected from floating point precision. For more complex composite profiles, including outer density terms and transfer functions, discrepancies increase modestly but remain well below the level of physical modeling uncertainties relevant for observational analyses.

A central outcome of this work is the validation of external implementations of outer halo components and of the DK14 profile when coupled to NumCosmo's internal machinery. These results provide a start for integrating such models directly into NumCosmo, being that a natural extension for future work. This step is important because once fully integrated, these profiles could be usable in cosmological pipelines such as the Cluster Lensing Mass Modeling (CLMM) library, which plays a key role in cluster mass calibration for weak lensing surveys.

The relevance of these developments is underscored by the current observational landscape. The Vera C. Rubin Observatory has recently achieved first light, marking the beginning of a new era in wide-field, time-domain astronomy. Over the coming years, data releases from the Rubin Observatory, analyzed in coordination by the LSST Dark Energy Science Collaboration (DESC), are expected to dramatically increase the statistical power of weak lensing and large scale structure measurements. In this regime, theoretical systematics, rather than statistical noise, will increasingly dominate the uncertainties.

It is, as always, an exciting time to be a cosmologist.

REFERENCES

Bibliography

[1] KiDS Collaboration et al. “KiDS-1000 cosmology: Cosmic shear constraints and comparison between two point statistics”. In: *Astronomy amp; Astrophysics* 645 (2021), A104. arXiv: 2007.15633 [astro-ph].

[2] DES Collaboration et al. “Dark Energy Survey Year 3 results: Cosmological constraints from galaxy clustering and weak lensing”. In: *Physical Review D* 105.2 (2022). ISSN: 2470-0029. DOI: 10.1103/physrevd.105.023520. arXiv: 2105.13549 [astro-ph]. URL: http://dx.doi.org/10.1103/PhysRevD.105.023520.

[3] HSC Collaboration et al. “Cosmology from cosmic shear power spectra with Subaru Hyper Suprime-Cam first-year data”. In: *Publications of the Astronomical Society of Japan* 71.2 (2019). arXiv: 1809.09148 [astro-ph].

[4] The LSST Dark Energy Science Collaboration et al. *LSST Science Book, Version 2.0*. 2009. arXiv: 1809.01669 [astro-ph.CO].

[5] Carlo Rovelli. *General Relativity: The Essentials*. Cambridge University Press, 2021.

[6] Daniel Baumann. *Cosmology*. Cambridge University Press, 2022.

[7] Planck Collaboration et al. “Planck 2018 results. VI. Cosmological parameters”. In: *Astronony & Astrophysics* 641 (2020), A6. arXiv: 1807.06209 [astro-ph.CO].

[8] European Space Agency (ESA) and the Planck Collaboration. *Planck’s view of the cosmic microwave background (CMB)*. https://www.esa.int/ESA_Multimedia/Images/2013/03/Planck_CMB. Accessed: 2025-11-20.

[9] L. Perivolaropoulos and F. Skara. “Challenges for Λ CDM: An update”. In: *New Astronomy Reviews* 95 (2022), p. 101659. arXiv: 2105.05208 [astro-ph.CO].

[10] Luiz Felipe Demétrio. “Quantum Perturbations in Bianchi Models”. PhD thesis. Universidade Estadual de Londrina, 2023. URL: https://pos.uel.br/fisica/wp-content/uploads/2025/06/Dissertacao-Luiz-Felipe-Demetrio-2023.pdf.

[11] Mario Novello and SE Perez Bergliaffa. “Bouncing cosmologies”. In: *Physics reports* 463.4 (2008), pp. 127–213.

[12] Abhay Ashtekar and Parampreet Singh. “Loop Quantum Cosmology: A Status Report”. In: *Class. Quant. Grav.* 28 (2011), p. 213001. DOI: 10.1088/0264-9381/28/21/213001. arXiv: 1108.0893 [gr-qc].

[13] DESI Collaboration, M. Abdul-Karim, et al. “DESI DR2 Results II: Measurements of Baryon Acoustic Oscillations and Cosmological Constraints”. In: *Physical Review D* 112 (2025), p. 083515. arXiv: 2503.14738 [astro-ph.CO].

[14] K. Lodha, DESI Collaboration, et al. "Extended Dark Energy analysis using DESI DR2 BAO measurements". In: (2025). arXiv: 2503.14743 [astro-ph.CO].

[15] T Padmanabhan. "Cosmological constant—the weight of the vacuum". In: *Physics Reports* 380 (2003), pp. 235–320. arXiv: 0212290 [hep-th].

[16] Gianfranco Bertone, Dan Hooper, and Joseph Silk. "Particle dark matter: evidence, candidates and constraints". In: *Physics Reports* 405.5–6 (2005), pp. 279–390. arXiv: 0212290 [hep-th].

[17] Lam Hui. "Wave Dark Matter". In: *Ann. Rev. Astron. Astrophys.* 59 (2021), pp. 247–289. DOI: 10.1146/annurev-astro-111720-030029. arXiv: 2101.11735 [astro-ph.CO].

[18] Alexey Boyarsky et al. "Sterile Neutrino Dark Matter". In: *Prog. Part. Nucl. Phys.* 104 (2019), pp. 1–45. DOI: 10.1016/j.ppnp.2018.07.004. arXiv: 1807.07938 [hep-ph].

[19] Carlos R. Argüelles et al. "Fermionic Dark Matter: Physics, Astrophysics, and Cosmology". In: *Galaxies* 11 (2023), p. 61. DOI: 10.3390/galaxies11030061. arXiv: 2304.06329 [astro-ph.GA].

[20] Marika Asgari, Alexander J. Mead, and Catherine Heymans. "The halo model for cosmology: a pedagogical review". In: *The Open Journal of Astrophysics* 6 (2023). arXiv: 2303.08752 [astro-ph.CO].

[21] William H. Press and Paul Schechter. "Formation of Galaxies and Clusters of Galaxies by Self-Similar Gravitational Condensation". In: 187 (1974), pp. 425–438.

[22] Benedikt Diemer. "COLOSSUS: A Python Toolkit for Cosmology, Large-scale Structure, and Dark Matter Halos". In: *The Astrophysical Journal Supplement Series* 239.2 (2018), p. 35. arXiv: 1712.04512 [astro-ph.CO].

[23] Eric Hayashi and Simon D. M. White. "Understanding the halo-mass and galaxy-mass cross-correlation functions". In: *Monthly Notices of the Royal Astronomical Society* 388.1 (2008), pp. 2–14. arXiv: 0709.3933 [astro-ph.CO].

[24] Matthias Bartelmann and Peter Schneider. "Weak gravitational lensing". In: *Physics Reports* 340.4–5 (2001), pp. 291–472. arXiv: 9912508 [astro-ph].

[25] Cameron Lemon et al. "Searching for Strong Gravitational Lenses". In: *Space Science Review* 220.23 (2024). arXiv: 1807.06209 [astro-ph.CO].

[26] Matthias Bartelmann and Matteo Maturi. *Weak gravitational lensing*. 2016. arXiv: 1612.06535 [astro-ph.CO]. URL: https://arxiv.org/abs/1612.06535.

[27] Albert Einstein. "Die Grundlage der allgemeinen Relativitätstheorie". In: *Annalen der Physik* 49 (1916), pp. 769–822. DOI: 10.1002/andp.19163540702.

[28] Rachel Mandelbaum. "Weak Lensing for Precision Cosmology". In: *Annual Review of Astronomy and Astrophysics* 56.1 (2018), pp. 393–433. arXiv: 1710.03235 [astro-ph].

[29] DES Collaboration et al. "Dark Energy Survey Year 3 results: Curved-sky weak lensing mass map reconstruction". In: *Monthly Notices of the Royal Astronomical Society* 505.3 (2021), pp. 4626–4645. arXiv: 2105.13539 [astro-ph].

[30] David J. Bacon, Alexandre R. Refregier, and Richard S. Ellis. "Detection of weak gravitational lensing by large-scale structure". In: *Monthly Notices of the Royal Astronomical Society* 318.2 (2000), pp. 625–640. arXiv: 0003008 [astro-ph].

[31] H. Hoekstra et al. "First Cosmic Shear Results from the Canada-France-Hawaii Telescope Wide Synoptic Legacy Survey". In: *The Astrophysical Journal* 647.1 (2006), pp. 116–127. arXiv: 0511089 [astro-ph].

[32] KiDS Collaboration et al. "KiDS-Legacy: Cosmological constraints from cosmic shear with the complete Kilo-Degree Survey". In: *Astronomy amp; Astrophysics* (2025). arXiv: 2503.19441 [astro-ph].

[33] The LSST Dark Energy Science Collaboration et al. *The LSST Dark Energy Science Collaboration (DESC) Science Requirements Document*. 2021. arXiv: 1809.01669 [astro-ph.CO].

[34] Vera C. Rubin and W. Kent Ford Jr. "Rotation of the Andromeda Nebula from a Spectroscopic Survey of Emission Regions". In: 159 (Feb. 1970), p. 379. DOI: 10.1086/150317.

[35] J. P. Ostriker, P. J. E. Peebles, and A. Yahil. "The Size and Mass of Galaxies, and the Mass of the Universe". In: *Astrophysical Journal* 193 (1974).

[36] Julio F. Navarro, Carlos S. Frenk, and Simon D. M. White. "A Universal Density Profile from Hierarchical Clustering". In: *The Astrophysical Journal* 490.2 (Dec. 1997), pp. 493–508. ISSN: 1538-4357. DOI: 10.1086/304888. URL: http://dx.doi.org/10.1086/304888.

[37] The LSST Dark Energy Science Collaboration et al. "CosmoDC2: A Synthetic Sky Catalog for Dark Energy Science with LSST". In: 245.2, 26 (Dec. 2019), p. 26. DOI: 10.3847/1538-4365/ab510c. arXiv: 1907.06530 [astro-ph.CO].

[38] Charles R. Keeton. *A Catalog of Mass Models for Gravitational Lensing*. 2002. arXiv: astro-ph/0102341 [astro-ph].

[39] H. Zhao. "Analytical models for galactic nuclei". In: *Monthly Notices of the Royal Astronomical Society* 278.2 (Jan. 1996), pp. 488–496. ISSN: 1365-2966. DOI: 10.1093/mnras/278.2.488. URL: http://dx.doi.org/10.1093/mnras/278.2.488.

[40] Lars Hernquist. "An Analytical Model for Spherical Galaxies and Bulges". In: 356 (June 1990), p. 359. DOI: 10.1086/168845.

[41] J. Einasto. "On the Construction of a Composite Model for the Galaxy and on the Determination of the System of Galactic Parameters". In: *Trudy Astrofizicheskogo Instituta Alma-Ata* 5 (Jan. 1965), pp. 87–100.

[42] C. Power et al. “The inner structure of ΛCDM haloes - I. A numerical convergence study”. In: 338.1 (Jan. 2003), pp. 14–34. DOI: 10.1046/j.1365-8711.2003.05925.x. arXiv: astro-ph/0201544 [astro-ph].

[43] Liang Gao et al. “The redshift dependence of the structure of massive Λ cold dark matter haloes”. In: 387.2 (June 2008), pp. 536–544. DOI: 10.1111/j.1365-2966.2008.13277.x. arXiv: 0711.0746 [astro-ph].

[44] Benedikt Diemer and Andrey V. Kravtsov. “Dependence of the Outer Density Profiles of Halos on Their Mass Accretion Rate”. In: 789.1, 1 (July 2014), p. 1. DOI: 10.1088/0004-637X/789/1/1. arXiv: 1401.1216 [astro-ph.CO].

[45] Benedikt Diemer. “A dynamics-based density profile for dark haloes - II. Fitting function”. In: 519.3 (Mar. 2023), pp. 3292–3311. DOI: 10.1093/mnras/stac3778. arXiv: 2205.03420 [astro-ph.CO].

[46] Thais M. Ornellas. “Relações de Concetração-Massa em Escalas de Grupos de Aglomerados de Galáxias: Impacto nas Restrições de Massa e de Parâmetros Cosmológicos”. MA thesis. Universide Estadual de Londrina, 2025.

[47] Sandro Dias Pinto Vitenti and Mariana Penna-Lima. *NumCosmo: Numerical Cosmology*. Astrophysics Source Code Library, record ascl:1408.013. Aug. 2014. ascl: 1408.013.

[48] Sandro Dias Pinto Vitenti and Mariana Penna-Lima. *NumCosmo: Numerical Cosmology*. Astrophysics Source Code Library, record ascl:1408.013. Aug. 2014. ascl: 1408.013.

[49] NumCosmo Developers. *NumCosmo: The Numerical Cosmology Library (Documentation)*. https://numcosmo.readthedocs.io/en/latest/. Version 0.26.0, accessed 2025-11-21. 2025.

[50] Benedikt Diemer. *Colossus — Documentation of the Colossus Python toolkit for cosmology, large-scale structure, and dark matter halos*. https://bdiemer.bitbucket.io/colossus/index.html. Accessed: 2025-11-21. 2025.

[51] M Aguena et al. “CLMM: a LSST-DESC cluster weak lensing mass modeling library for cosmology”. In: *Monthly Notices of the Royal Astronomical Society* 508.4 (Oct. 2021), pp. 6092–6110. ISSN: 1365-2966. DOI: 10.1093/mnras/stab2764. URL: http://dx.doi.org/10.1093/mnras/stab2764.